The Astronomical Journal, 135:693–721, 2008 February doi:10.1088/0004-6256/135/2/693

X-RAY AND IR POINT SOURCE IDENTIFICATION AND CHARACTERISTICS IN THE EMBEDDED, MASSIVE STAR-FORMING REGION RCW 108

Scott J. Wolk[1], Bradley D. Spitzbart[1], Tyler L. Bourke[1], Robert A. Gutermuth[1], Miquela Vigil[2], and Fernando Comerón[3]
[1] Harvard–Smithsonian Center for Astrophysics, 60 Garden Street, Cambridge, MA 02138, USA
[2] Lincoln Laboratory, Massachusetts Institute of Technology, Lexington, MA 02420, USA
[3] European Southern Observatory, Karl-Schwarzschild Strasse 2, D-85748 Garching bei München, Germany
Received 2007 April 11; accepted 2007 October 5; published 2008 January 17

ABSTRACT

We report on the results of an approximately 90 ks *Chandra* observation of a complex region that hosts multiple sites of recent and active star formation in ARA OB1a. The field is centered on the embedded cluster RCW 108–IR and includes a large portion of the open cluster NGC 6193. We detect over 420 X-ray sources in the field and combined these data with deep near-IR, *Spitzer*/IRAC and *Midcourse Space Experiment* (*MSX*) mid-IR data. We find about 360 of the X-ray sources have near-IR counterparts. We divide the region into five parts based on the X-ray point source characteristics and extended 8 μm emission. The most clearly defined regions are the central region, identified by embedded sources with high luminosities in the both the near-IR and X-ray as well as high X-ray temperatures ($\sim$3 keV), and the eastern region, identified by low extinction and $\sim$1 keV X-ray temperatures. Other regions, identified by their directional relationship to RCW 108–IR, are less uniform—representing combinations of the first two regions, independent star formation epochs, or both. The cluster members range in X-ray luminosity from 10^{29} to 10^{33} erg s^{-1}. Over 18% of the cluster members with over 100 counts exhibit flares. All sources with over 350 counts are variable. Overall about 10% (16% in RCW 108–IR) appear to have optically thick disks as derived from their position in the $(J - H)$, $(H - K)$ diagram. The disk fraction becomes much higher when IRAC data are employed. The largest fraction of X-ray sources is best described as possessing some disk material via a more detailed extinction fitting. We fit the bulk of the X-ray spectra as absorbed Raymond–Smith-type plasmas, and find that the column to the RCW 108–IR members varies from 10^{21} to 10^{23} cm^{-2}. We find that the field contains 41 candidate O or B stars, and estimate that the total number of pre–main-sequence stars in the field is about 1600 $\pm$ 200. Approximately 800 are confined to the 3′ ($\sim$1.1 pc) central region.

Key words: H II regions – ISM: individual (RCW 108) – stars: formation – X-rays: stars

Online-only material: color figure, machine-readable tables

1. INTRODUCTION

Ara OB1a may be one of the best examples of triggered star formation in the local Galaxy. The triggering in the most active portion is easily imagined from images of the NGC 6193/RCW 108–IR complex, such as Figure 1. Ara OB1 was first studied in detail by Whiteoak (1963) using photographic photometry and objective prism spectroscopy to identify about 35 O and B star members. He identified OB1a with a relatively nearby cluster associated with open clusters NGC 6193 and NGC 6167, while Ara OB1b was found to be about twice as distant. Whiteoak's work was a follow-up to an Hα survey by Rodgers et al. (1960; RCW), who cataloged 181 Hα emission regions in the southern sky. NGC 6193 is an open cluster dominated by a pair of O stars, HD 150135 (O6.5V; Walborn 1972) and HD 150136 (O3+O6V; Niemela & Gamen 2005). These are the brightest optically revealed O stars in the association and are thought to be responsible for ionizing the bright rim of emission to the west (NGC 6188), which separates NGC 6193 from RCW 108. The youth of the region is clear in sky survey plates and Figure 1 which show concurrent regions of ionized gas and dust lanes.

Ara OB1a is a compact association covering about 1 sq. degree ($\sim$25 pc on a side) around a central cluster, NGC 6193. The distance to NGC 6193 is 1.3 $\pm$ 0.2 kpc, and the cluster is associated with the H II region RCW 108 (Herbst & Havlen 1977). There is some confusion in the literature as to what is actually meant by RCW 108. The original definition of Rodgers et al. (1960) refers to the whole region where Hα nebulosity is detected, for which they give a size of 210′ × 120′ centered at $l, b = 336.49, -1.48$. Straw et al. (1987) used RCW 108–IR to refer to the embedded IR cluster about 15′ to the west of the O stars in NGC 6193 that has been identified with IRAS 16362-4845. The confusion arises when RCW 108–IR is abbreviated by dropping the "-IR." For the remainder of this paper we will refer to the embedded cluster as RCW 108–IR.

1.1. NGC 6193

NGC 6193 is the open cluster to the east of the bright emission rim NGC 6188. In a region about 40′ ($\sim$15 pc) on a side, Herbst & Havlen (1977) measured over 700 stars photometrically. Of these, 59 had photometric distances and reddening consistent with cluster membership. Their survey appears complete to spectral types earlier than A0. Their best fit to the photometric distance was 1,320 $\pm$ 120 pc. Several other groups have estimated the distance to the cluster using photometric parallax techniques, and obtained results ranging from $\approx$1,100 pc to $\approx$1,400 pc (Moffat & Vogt 1973; Fitzgerald 1987; Kalcheva & Georgiev 1992). Vazquez & Feinstein (1992) obtained an age of about 3 Myr by fitting the upper main sequence; they also determined a distance of about 1,410 $\pm$120 pc. We will use 1.3 kpc for this paper to be consistent with recent studies. For linear distances we will usually use parsecs, 1′ = 0.38 pc at 1.3 kpc. The mean extinction is low toward NGC 6193 ($A_V \sim 0.5$).

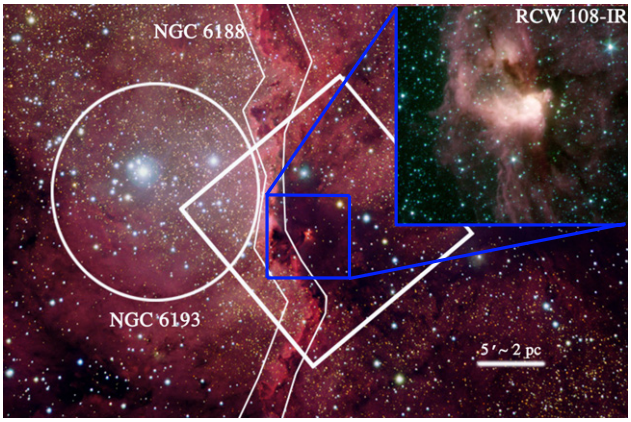

Figure 1. Optical image of the RCW 108 region (adapted from image by Robert Gendler and Martin Pugh 2006; http://www.robgendlerastropics.com/NGC6188MP.html). The ACIS-I field of view is outlined as a square about 17′ on a side. The bright stars to the east are the HD 150135/6 complex of O stars. These stars are the center of NGC 6193 (circle); NGC 6188 is identified as the ridge of emission. The inset shows an IRAC image of RCW 108–IR showing the detail of the ionization front (BGOR = 3.6 μm, 4.5 μm, 5.8 μm, and 8.0 μm, respectively). The edge of the diffuse emission is fairly sharp.

From the X-ray perspective, there is an image from the zero order of a 100 ks *Chandra* observation (Skinner et al. 2005). Since the effective area of the HETG zero order is only about 15% that of the unobscured ACIS-I, this observation is relatively shallow. Still, the observation should be fairly complete to 1 solar mass. It reveals 43 X-ray sources in the central square 0.76 pc on a side. Only 11 of these had previous optical identifications; however, all 43 were detected at *H* band by the Two Micron All Sky Survey (2MASS), and are likely cluster members. In addition to those sources cataloged by Skinner et al., there are about 30 X-ray point sources visible outside of the central 0.8 pc on a side region in this data set. Most of these have *I*-band magnitudes consistent with cluster membership, and are between 0.8 pc and 2.58 pc from HD 150136.

1.2. RCW 108–IR

A bright rim (NGC 6188) marks the border between the H II region and a dark nebula containing RCW 108–IR. The bright rim is produced by the ionization of the molecular cloud hosting RCW 108–IR by the two central stars of NGC 6193. Herbst & Havlen (1977) proposed this was a site of active star formation.

RCW 108–IR is a young, compact cluster partially embedded in its parent molecular cloud. Straw et al. (1987) used photometry at IR wavelengths (1.2–100 μm) to perform the first survey of the cluster. They reported on 55 objects, of which <20 have optical counterparts. In addition to the point sources, there is diffuse IR emission. The total luminosity of the cluster is about $1.8 \times 10^5 L_\odot$, dominated by two early O stars. The full aggregate of O and B stars appears responsible for the ionization of the diffuse emission (Comerón et al. 2005). The primary exciting source star, identified by Straw et al. as IRS 29, is resolved into multiple sources by Comerón et al. The brightest of these is a probable O9 star. Straw et al. also identify at least 1 protostar based on high luminosity and low temperature. They put forward a physical model of the region in which photoionization of the older stars in the Ara OB1a association ionized the bright rim (NGC 6188) which lies at the edge of a finger of molecular material which thickens from east to west. IRS 29 is the second-strongest water maser seen by the *Submillimeter Wave Astronomy Satellite* (*SWAS*) (second to the BN object on Orion; Melnick, private communication) with a peak flux of over 7000 Jy in the 557 GHz line. A follow-up study suggests that gaseous H_2O is largely restricted to a thin layer of gas near the cloud surface.

There have been two recent near-IR through mm studies of RCW 108–IR. Urquhart et al. (2004) compared the 2MASS and *Midcourse Space Experiment* (*MSX*) observations of the cloud with radio recombination lines and radio continuum using the Australia Telescope Compact Array (ATCA). With synthesized beamwidths of 12–20″, they find RCW 108–IR is an ultracompact H II region, less than 0.1 pc in scale with a core–halo morphology. They discuss eight new sources within the UCHII region and three 25 μm sources set back about 0.95 pc from the bright rim. A more detailed study has been recently published by Comerón et al. (2005). From their high resolution (~25″) CO map they estimate a total mass of the cloud at 8,000 $M_\odot$ with < 200 $M_\odot$ in the molecular concentration harboring the compact H II region. They produced a high resolution JHK_s map of the region, and identified 25 stars whose luminosities suggest spectral types earlier than A0 under the assumption that there is no significant circumstellar contribution to the *K*-band flux within the diffuse IR nebula. Comerón et al. conclude that the ionization of the UCHII region is provided by this aggregate. Strangely, they detect no stars later than A0 in the core. They suggest that low-mass star formation has yet to commence here. Deeper adaptive optics imaging does reveal fainter members of the cluster, but not in the large numbers that would have been expected from an extrapolation of the *K* luminosity function of the brightest members toward fainter magnitudes (Comerón & Schneider 2007). IRS 29 is found to be an O9 star from the visible spectrum of the compact H II nebula, which is in agreement with its infrared photometry. Urquhart et al. (2004) confirm the O9 spectral type via radio flux measurements. Out of 4365 stars brighter than $K_s = 14.5$ in the whole $13' \times 13'$ field (~5 pc on a side), 87 are found to have strong disk signatures, most being located in the molecular cloud that contains RCW108–IR and along the inside of the bright rim, NGC 6188.

We recently observed RCW 108–IR, the southwestern portion of NGC 6193, and the dividing rim NGC 6188 using the *Chandra* X-ray Observatory. The goals of the observation were to (i) detect the effects of triggered star formation, (ii) identify deeply embedded pre–main-sequence (PMS) stars via their X-ray emission and derive an initial mass function and an X-ray luminosity function, and (iii) investigate the X-ray properties of the embedded sources. In Section 2, we outline the X-ray observations made specifically for this paper and supporting IR and mm wave observations. In Section 3, we combine these data to understand the basic morphology of the region, dividing the field into five regions based on a core region and the cardinal directions which are well aligned to NGC 6188. The X-ray characteristics of the X-ray sources and their regional dependencies are discussed in the next two sections. In Section 6, near-IR and mid-IR data are brought in to study the gas-to-dust ratio, *K*-band luminosity functions, and OB stars among the X-ray sources. The more extreme X-ray sources are discussed in Section 7. We compare our work with other recent results in Section 8, and summarize our results in Section 9.

2. OBSERVATION AND DATA REDUCTION

This paper will focus on X-ray observations of RCW 108–IR and NGC 6193 made by *Chandra*. But we will also incorporate several other observations, many of which have not been

Table 1
Bright X-ray Sources Detected in the RCW 108 Field

SRC #	CXOWSBJ	R.A. (J2000.0)	Decl. (J2000.0)	Offaxis (arcsec)	Counts [Raw]	Counts [Net]	BB95[a]
1	164036.6–485217.3	16:40:36.64	−48:52:17.37	375.2	130	112.7	1
2	164035.8–485106.7	16:40:35.82	−48:51:06.76	369.5	187	169.8	1
3	164034.9–485049.5	16:40:34.90	−48:50:49.52	363.2	95	79.3	1
4	164033.3–485023.6	16:40:33.32	−48:50:23.67	353.6	666	661.5	4
5	164032.1–485323.0	16:40:32.14	−48:53:23.02	341.8	23	17.5	1
6	164031.9–484913.0	16:40:31.90	−48:49:13.06	365.2	59	43	1
7	164031.8–485312.4	16:40:31.89	−48:53:12.42	336.7	138	133.2	1
8	164031.4–485311.9	16:40:31.44	−48:53:11.95	332.3	152	147.1	2
9	164031.2–485211.5	16:40:31.23	−48:52:11.56	321.6	59	51.8	1
10	164031.0–485249.6	16:40:31.07	−48:52:49.68	324.2	61	55.7	1
11	164030.9–484938.0	16:40:30.92	−48:49:38.04	346.1	33	27.9	1
12	164030.6–485215.6	16:40:30.67	−48:52:15.61	316.3	738	730.8	6
13	164030.6–485026.4	16:40:30.66	−48:50:26.41	327.5	37	31.3	1
14	164030.2–485108.3	16:40:30.20	−48:51:08.36	314.4	43	38.3	2
15	164030.1–484957.8	16:40:30.12	−48:49:57.82	331.4	18	12.7	2

Note.
[a] BB95 = The number of Bayesian Blocks of greater than 95% confidence required to describe the lightcurve. Any number >1 indicates variability at 95% confidence.
(This table is available in its entirety in a machine-readable form in the online journal. A portion is shown here for guidance regarding its form and content)

discussed in the published literature. The observations include near-IR photometry, mid-IR observations by *Spitzer*/IRAC and *MSX*, as well as mm wave observations performed at the Swedish-ESO Submillimetre Telescope (SEST). After detailing the reduction of the primary X-ray data, the other data reduction is summarized in this section.

2.1. X-Ray Data

The field was observed by *Chandra* on 2004 October 25 starting at 02:37 UT for 92.2 ks of total time and 88.8 ks of so-called "good-time" (ObsId 4503). The ACIS was used in the nominal imaging array (chips I0-I3) which provides a field of view of approximately $17' \times 17'$ (∼6.5 pc on a side). The aimpoint was at 16:39:58.7, −48:51:54.4 (J2000.0) . In addition, the S2 and S3 chips were on and located over IRAS 16379–4856. About 20 point sources were detected associated with this object; however, the analysis of these data is not presented here because they are far off-axis.

The background was slightly variable during this observation. For the first 5 ks the background was about 5% higher than the median, and a similar high period which lasted about 2 ks occurred about 20 ks into the observation. The background was about 3% lower than the median for the last 10 ks. The data used in these analysis were reprocessed using the default "repro 3" provided by the *Chandra* X-ray Center (CXC) data systems. As such, they were processed through the standard CIAO pipeline at the CXC, using their version DS7.6. This version of the pipeline automatically incorporated a noise correction for low-energy events. It has been noted that this filter can remove good events from the cores of bright point sources, resulting in an underestimation of the X-ray flux (L. Townsley, private communication). This proved not to be an issue in this case since the count rate did not exceed 0.04 counts per second for any source.

To identify point sources, photons with energies below 300 eV and above 8.0 keV were filtered out. The excluded energies generally lack a stellar contribution due to the low instrumental throughput and the relatively cool thermal spectra of coronal emission. By filtering the data as described, contributions from hard, non-stellar sources and monochromatic detector background are attenuated. A monochromatic exposure map was generated in the standard way using an energy of 1.49 keV which is a reasonable match to the expected peak energy of the sources and the *Chandra* mirror transmission. WavDetect was then run on a series of flux corrected images binned by 1, 2, and 4 pixels. The resulting source lists were combined and this resulted in the detection of 429 sources. For the bulk of the X-ray analysis we will restrict ourselves to the 337 source detections with significance greater than 3.5.[4] These are tabulated in Table 1. However, all X-ray sources returned by WavDetect are statistically significant and we present follow-up information on the faint sources as well. The fainter sources are listed in Table 2. In each of these tables, the first column contains a running SRC number, the second an official IAU style designation. Columns 3 and 4 are the R.A. and declination of the centroid of the X-ray source followed by the off axis angle in Column 5. At each source position an extraction ellipse was calculated following Wolk et al. (2006) updated for the appropriate satellite roll angle.[5] This provides an extraction ellipse containing 95% of the source flux. The numbers of counts in this region are listed in Column 6. For each of the 429 sources, a background ellipse is identified. The background is an annular ellipse with the same center, eccentricity, and rotation as the source. The outer radius is six times the radius of the source, and the inner radius is three times larger than the source. From this region any nearby sources are subtracted with ellipses three times the size of the source ellipse. The net counts are calculated by subtracting the background counts (corrected for area) and multiplying the result by 1.053 to correct for the use of a 95% encircled energy radius. This is the value given in Column 7.

[4] The src_significance given by the CIAO tool WavDetect is not in units of σ so no false alarm probability is associated. While the relative value of src_significance is meaningful, it is not clearly defined in a statistical sense (V. Kashyap, private communication).
[5] *Chandra* roll angle is the angle between the detector vertical and north. The point-spread function is strongly dependent on *both* the off-axis angle (Θ) and the rotation angle (Ψ) of the incident point source.

Table 2
Faint X-ray Sources Detected in the RCW 108 Field

SRC #	CXOWSBJ	R.A. (J2000.0)	Decl. (J2000.0)	Offaxis (arcsec)	Src sig.	Counts [Net]
401	164028.1–484956.6	16:40:28.109	−48:49:56.59	313.2	3.1	8.1
402	164027.4–485040.1	16:40:27.481	−48:50:40.14	293.4	2.1	5.0
403	164027.3–485116.9	16:40:27.339	−48:51:16.89	285.0	1.9	4.2
404	164026.2–484749.1	16:40:26.210	−48:47:49.05	366.0	3.0	8.5
405	164022.5–485512.0	16:40:22.533	−48:55:11.96	307.2	2.2	5.0
406	164022.4–485231.4	16:40:22.425	−48:52:31.37	237.0	2.5	5.9
407	164022.3–485650.1	16:40:22.357	−48:56:50.06	376.8	3.0	9.4
408	164022.0–485025.4	16:40:22.038	−48:50:25.39	247.2	2.8	6.8
409	164021.0–485202.1	16:40:21.037	−48:52:02.06	220.8	2.1	5.0
410	164019.9–484945.7	16:40:19.991	−48:49:45.75	246.6	2.8	6.8
411	164019.6–485314.3	16:40:19.635	−48:53:14.30	221.4	3.1	7.1
412	164018.8–485317.6	16:40:18.827	−48:53:17.69	215.4	2.3	5.2
413	164015.1–485141.6	16:40:15.188	−48:51:41.64	163.2	3.3	8.4
414	164013.3–484853.1	16:40:13.316	−48:48:53.11	231.6	3.0	7.0
415	164010.9–484742.8	16:40:10.964	−48:47:42.86	279.0	2.2	4.6

(This table is available in its entirety in a machine-readable format. A portion is shown here for guidance regarding its form and content)

Table 3 contains a cross-referencing for all X-ray sources with a counterpart found in the SIMBAD database with an offset of $<2''$.

2.2. MSX Observations

The MSX obtained observations of RCW 108–IR and its surroundings at 8.3, 12.1, 14.7, and 21.3 μm as part of its Galactic plane survey (Price et al. 2001). The four bands are labeled *A* (6.8–10.8 μm), *C* (11.1–13.2 μm), *D* (13.5–15.9 μm), and *E*(18.2–25.1 μm). The *A* and *C* band emission is a combination of thermal dust emission and emission from polycyclic aromatic hydrocarbon (PAH) bands at 7.7, 8.6, and 11.2 μm. The *D* and *E* bands trace thermal emission of cool dusty objects. The details of the reduction of these data are discussed by Price et al. (2001).

2.3. Near-IR Observations

In the near-IR we use J, H, and K_s photometry obtain from 2MASS project and from a deep pointed observation of RCW 108–IR. The latter data are discussed by Comerón et al. (2005), while the 2MASS point source catalog reductions are summarized by Cutri et al. (2003). $J\,H\,K_s$ photometry of sources in the central region of RCW 108–IR is taken from deep adaptive optics observations carried out with the VLT and described in Comerón and Schneider (2007). We will discuss the details of the matching of the near-IR point sources and X-ray sources in Section 6.

2.4. Spitzer/IRAC Observations

RCW 108–IR was observed with the Infrared Array Camera (IRAC; Fazio et al. 2004) on board the *Spitzer* Space Telescope (Werner et al. 2004). A very shallow IRAC map of RCW 108–IR and the surrounding region was made as part of the *Spitzer* "Early Release Observations." These were very limited programs primarily with aesthetic, not scientific, goals. The mean exposure was about 3.2 s per band and total observing time of about 30 min. Observations were made in 2005 September (PID 112). The total area covered with four-band coverage was roughly $23'$ ($\sim$8.75 pc) on a side, aligned roughly north–south. Two-band coverage extends $5'$ to the north and south—band 2/4 ((4.5 μm) and (8.0 μm), respectively) in the north and band 1/3 ((3.6 μm) and (5.8 μm), respectively) in the south. Mosaics and related data were downloaded from the *Spitzer* archive in software version S12.4.0. Additional processing to remove artifacts and perform point source photometry was performed using customized software described by Gutermuth et al. (2007; PhotVis, see Section 2.1). Sources were then classified into infrared disk class (c.f. Lada & Adams 1992; Allen et al. 2004; Megeath et al. 2004) following the prescription in Gutermuth et al. (2007; Section 4.1) which uses cuts in a multidimensional color space including J, H, K_s, and all four IRAC bands. About 2,600 sources were detected in all four bands within the full IRAC field. About 20,000 sources were detected in at least one IRAC band. Diffuse emission is clear in the 5.8 and 8.0 μm bands and traces the lower-resolution *MSX* data.

2.5. Millimeter-Wave Observations

Observations at 1.2 mm were obtained in 2002 September and 2002 November with the 37-channel hexagonal bolometer array SIMBA at the SEST, located in La Silla, Chile at an altitude of 2,370 m. The SEST, now defunct, was a 15 m diameter telescope and operated in the frequency range 70–365 GHz with a typical pointing accuracy of $3''$ in azimuth and elevation. The HPBW of a single SIMBA element was about $24''$, and the separation between elements in the sky is $44''$. In the final maps, pixels were $8''$ on a side with a beamwidth of $24''$ and a sensitivity of 235 mJy/beam rms. SIMBA was set to fast scanning mode and the size for each map was $20'\times 20'$ with a scanning speed of $160''$ s^{-1}. Four maps were made of RCW 108 with different scanning angles. The data reduction and analysis was carried out using the MOPSI[6] software package (Chini et al. 2003).

3. MORPHOLOGY

It is clear from Figure 2 that the X-ray sources toward the center are harder than those toward the outside. Further, there is a remarkable hourglass-shaped region, $\sim$3 pc in extent,

[6] Mapping On-Off Pointing Skydip is a software package for infrared, millimeter, and radio data reduction developed and constantly upgraded by R. Zylka.

Table 3
Cross-Reference of X-ray Sources with SIMBAD Counterparts Detected in the RCW 108 Field

SRC #	CXOWSB J	R.A.[a]	Decl.[a]	Alt. name	Ref.	Alt. name	Ref.	Alt. name
92	164006.2–485111	16:40:06.1	−48:51:12	IRS 27	SHJ87[b]			
95	164005.9–485111	16:40:06.1	−48:51:12	IRS 27	SHJ87[b]			
96	164005.7–485213	16:40:05.6	−48:52:12	IRS 9	SHJ87			
99	164004.7–485152	16:40:04.8	−48:51:53	IRS 20	SHJ87			
100	164004.4–485145	16:40:04.3	−48:51:45	IRS 22	SHJ87			
101	164003.8–485254	16:40:03.82	−48:52:54.7	Star q	UTM04			
107	164001.8–485137	16:40:01.8	−48:51:39	star 23	CSR05			
109	164001.6–485153	16:40:01.7	−48:51:53	star 22	CSR05			
111	164001.2–485145	16:40:01.3	−48:51:45	star 19	CSR05			
112	164001.1–485152	16:40:01.2	−48:51:52	star 18	CSR05			
114	164000.8–485138	16:40:00.9	−48:51:39	star 17	CSR05			
116	164000.3–485143	16:40:00.4	−48:51:43	star 16	CSR05			
118	164000.1–485139	16:40:00.2	−48:51:40	IRS 29	SHJ87	star 12	CSR05	
120	164000.0–485142	16:40:00.1	−48:51:42	star 10	CSR05	star 462	HH77	
121	163959.9–485153	16:40:00.0	−48:51:53	star 9	CSR05			
124	163959.7–485159	16:39:59.8	−48:52:00	star 7	CSR05			
125	163959.5–485137	16:39:59.6	−48:51:37	star 5	CSR05			
127	163959.3–485127	16:39:59.2	−48:51:27	IRS 42	SHJ87			
130	163958.5–485236	16:39:58.5	−48:52:36.8	star i	UTM04			
131	163958.5–485204	16:39:59.6	−48:52:05	star 2	CSR05			
136	163956.0–485148	16:39:55.98	−48:51:48.2	star f	UTM04			
138	163954.4–485201	16:39:54.5	−48:52:01.4	star e	UTM04			
140	163953.7–485145	16:39:53.7	−48:51:46.2	star d	UTM04			
145	163951.8–485141	16:39:51.83	−48:51:41.6	star b	UTM04			
174	163930.6–485102	16:39:30.67	−48:51:02.5	HD 149834				
215	163936.3–484755	16:39:36.39	−48:47:55.2	08333–00232	GSC	star 593	HH77	
217	163926.1–485147	16:39:26.10	−48:51:47.6	08333–01365	GSC	star 581	HH77	CPD-48 8655
243	164043.6–484851	16:40:43.61	−48:48:51.8	08333–00420	GSC	star 608	HH77	CD-48 11055
245	164041.0–485112	16:40:40.98	−48:51:21.1	08333–00814	GSC	star 226	HH77	
259	164016.0–485816	16:40:16.06	−48:58:15.8	08333–00074	GSC	star 536	HH77	CD-48 11044
267	164005.9–485908	16:40:05.89	−48:59:08.8	08333–00240	GSC	star 540	HH77	CD-48 11040
306	164039.0–484843	16:40:39.08	−48:48:44.3	08333–01125	GSC	star 625	HH77	
418	164006.5–485214	16:40:06.6	−48:52:15	IRS 8	SHJ87			
427	164000.1–485214	16:40:00.1	−48:52:16	IRS 6	SHJ87			

Notes.
[a] SIMBAD position.
[b] Both X-ray sources ∼1.8″ from IRS 27.
References. SHJ87 = Straw et al. (1987), UTM04 = Urquhart et al. (2004), CSR05 = Comerón et al. (2005), HH77 = Herbst & Havlen (1977), GSC = Guide Star Catalog (Lasker et al. 1990).

virtually devoid of sources except for those sources in the core. This is indicative of tremendous extinction. In this section, we investigate the relationship of this extinction to mid-infrared emission as observed by *MSX* and mm emission seen in the SEST observations. We also study whether the X-ray sources to the south and west are similar to those to the north and east. This would be expected if RCW 108–IR sits in a dark cloud in front of the larger NGC 6193 cluster and if sources from the older, more revealed cluster are seen around all sides of RCW 108–IR.

3.1. Long-Wavelength Morphology

The most extensive mid-IR emission is seen in the *MSX A* band data (Figure 3). These data show linear emission running south to north through the ACIS field, coincident with NGC 6188. The emission has a very sharp edge on the east side where the emission rises by a factor of about 3 (to about 4×10^{-6} W m^{-2} sr^{-1}) over a single resolution element. Emission levels remain elevated throughout the western two-thirds of the ACIS field. The *A* band emission peak is nearly coincident with the O star within the IRS 29 complex at 4.5×10^{-4} W m^{-2} sr^{-1}. *MSX C* and *D* band data trace the *A* band data at about 2/3 and 1/5 the irradiance level, respectively. Since the *D* band excludes PAH emission, this indicates that the emission is dominated by thermal dust.

The morphology of *MSX E*-band emission roughly follows the *A*-band emission. However, the 21 μm emission is concentrated in one fairly circular clump coincident with a concentration of emission at 1.2 mm. The extent of the 21 μm emission is about the same as the *A*-band emission in the east–west direction, and about 1 pc less in the north–south direction (in radius). The resolution in the *A* and *E* bands is about 20″; hence the *E* band emission is truly more circular. The *MSX E*-band emission does not show evidence of the dust ridge; however, the core region is bright. In addition to the south–north ridge (NGC 6188) and the core region (RCW 108–IR), there are three local maxima that are clear in all four bands. Table 4 lists the intensity of the emission in the various regions as observed by *MSX*. The *IRAS* data are included for completeness; however, *IRAS* did not resolve RCW 108–IR.

RCW 108–IR was observed at 1.2 mm to investigate the cold dust emission and morphology. Figure 4 shows an NTT K_s-band image of RCW 108 with 1.2 mm contours. The stellar population coincident with the 1.2 mm emission is extremely

Table 4
MSX and *IRAS* Intensity of RCW 108

Region	Area (arcsec^2)	*MSX* A (Jy)	*IRAS* 12 μm (Jy)	*MSX* C (Jy)	*MSX* D (Jy)	*MSX* E (Jy)	*IRAS* 25 μm (Jy)
A	3,996	6.81		8.74	4.10	11.39	
B	2,268	6.40		7.98	4.42	20.29	
C	1,080	2.72		3.97	2.06	3.96	
Core	2,844	101.37		216.6	326.0	2,063.4	
Entire	187,416	286.31	208.3	510.2	489.0	2,999.2	2,978

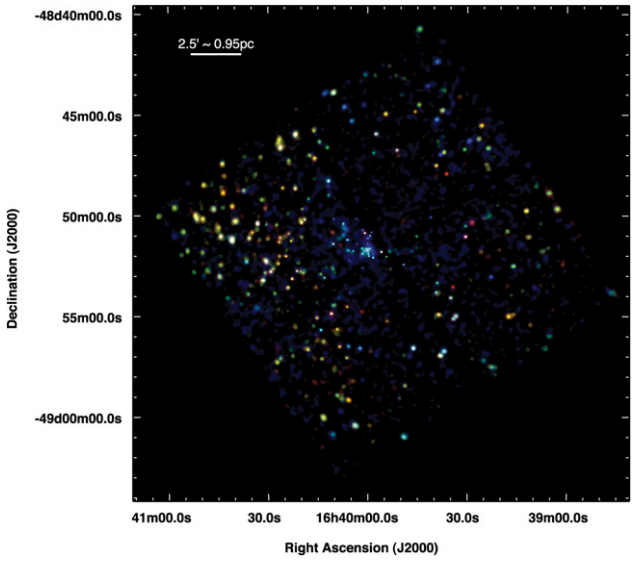

Figure 2. Adaptively smoothed version of the X-ray data. Photon energies between 300 eV and 1.1 keV are plotted in red, 0.9–2.4 keV in green and 2.1–8.0 keV in blue. Note the concentration of blue sources in the middle and a marked absence of source to the north and the south of this core. The eastern region has a multitude of sources at a variety of colors.

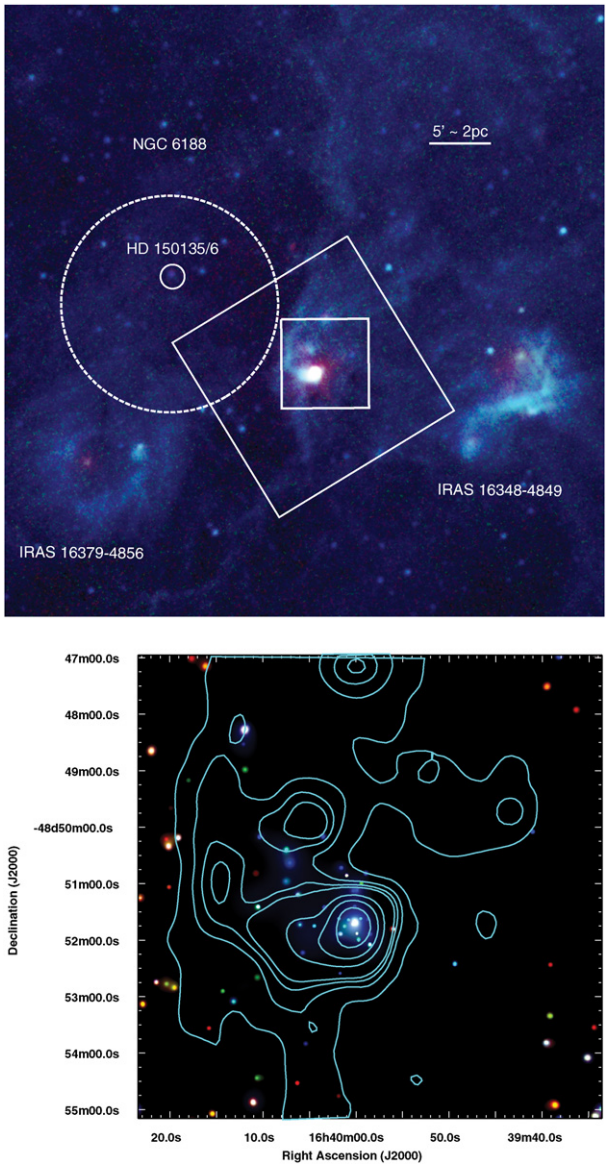

Figure 3. Top: an *MSX* image of approximately the same area as Figure 1. (BGR = *A* Band (8.28 μm), *C* band (12.13 μm), and *E* band (21.3 μm), respectively.) Two *IRAS* sources in the region are identified. The smaller box coincides with RCW 108–IR, shown in the lower panel. Bottom: a smoothed X-ray image of the central 3 pc × 3 pc region of RCW 108–IR (RGB = 0.5–1.1 keV, 0.9–2.4 keV, and 2.1–8.0 keV, respectively). The bright source near the center is IRS 29, an O9 star. The contours represent *MSX* A-band data at 4.7×10^{-6}, 8.9×10^{-6}, 1.3×10^{-5}, 1.7×10^{-5}, 5×10^{-5}, 1×10^{-4}, and 2×10^{-4} W m^{-2} sr^{-1}.

sparse, probably obscured by dust. However, several bright sources can be seen clustered near the peak of the 1.2 mm emission. The peak of the dust emission coincides with the central stellar population in the K_s-band image. The extension to the south is not coincident with any visible or X-ray source. The ^{13}CO data from Comerón et al. (2005) are peaked at the same location, slightly offset from the brightest near-IR sources and have a similar aspect ratio. However, the long axis of the ^{13}CO emission runs from the northwest to the southeast.

We compare the dust emission to mid-IR observations to understand the interactions between the different components of the regions, specifically the cold dust traced by the 1.2 mm emission and the warmer dust traced by the *MSX* mid-IR observations. The 1.2 mm emission is concentrated in a linear ridge running northeast to southwest, about 0.75 pc west of NGC 6188, approximately 1 pc in length with an extension to the east at the southern edge. From Figure 4, the north–south extent of the 1.2 mm emission is approximately 0.6 parsecs. The cold dust emission from RCW 108 is concentrated around one region without any secondary clumps and only the slight extension in the south. The peak emission is about 5 Jy at the center of the ridge. The bulk of the emission is within a ridge with the 21 μm emission extending slightly more toward the east than the 1.2 mm emission. The morphology of RCW 108 at 1.2 μm, 10–20 μm, and 1.2 mm show the bulk of the emission concentrated in one location near RCW 108–IR.

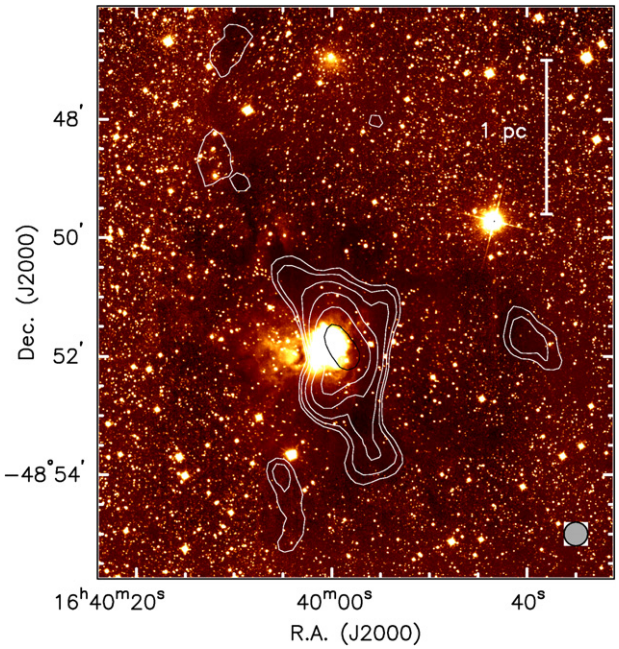

Figure 4. RCW 108 with 1.2 mm contours are 3, 6, 12, 24, 48, 96, 192 × σ (235 mJy/beam). The contours are overlain on the NTT K_s band image of Comerón et al. (2005). The beam size for the 1.2 mm observation is shown at the lower right.

(A color version of this figure is available in the online journal)

Color temperatures were derived from the ratios of the fluxes of the *MSX* bands assuming the regions followed a blackbody energy distribution. The contamination of the *A* band from PAH emission leads to unexpectedly high ratios; thus the color temperature of 224 K was calculated using the C/D ratio. This indicates that the warmer dust is externally heated, probably by photoionization from the O stars in NGC 6193. Meanwhile the dense dust in the center of RCW 108–IR remains thermally shielded even from the stars forming within it, with dust temperatures ∼20 K.

3.2. Dust Emission and Mass

The dust mass and density distribution in the molecular cloud was calculated using the 1.2 mm emission. Dust masses were calculated using the relation below, assuming the emission is optically thin ($\tau \sim 1$ at 1.3 mm when $N_{H2} \sim 10^{26}$ cm^{-2}; Hildebrand 1983; Mezger 1994):

$$M_{\rm dust} = \frac{S_\nu D^2}{\kappa_{\nu,d} B_\nu(T_d)} \quad (1)$$

where D is the distance to the cluster, S_ν is the observed dust emission, $\kappa_{\nu,d}$ is the dust opacity per unit mass column density, and $B_\nu(T_d)$ is the Planck function for a dust temperature T_d (Chini et al. 2003). The masses were calculated assuming a dust temperature of 20 K for the cold dust the SEST observations are sensitive to. While there are a range of possible dust opacities, we chose 0.37 cm^2 g^{-1} (Chini et al. 2003) which is a value consistent for the diffuse interstellar medium (ISM) but may increase by up to a factor of 10 in dense regions or protostellar environments (Ossenkopf & Henning 1994).

The vast majority of the 1.2 mm emission from RCW 108 is concentrated in one extended feature. The total mass of the region was determined from the flux within a contour of 30% of the maximum flux in the region which is 29.5 ± 0.4 Jy. The total dust mass was determined to be 23.1 ± 4.8 solar masses of cold dust. This gives a total mass of about 2300 $M_\odot$ assuming a gas-to-dust ratio of about 100.

3.3. X-Ray Morphology

The typical method of model-independent spectral analysis is to use X-ray colors in the form of hardness ratios, HR = (Cts$_{\rm h}$ − Cts$_{\rm s}$)/(Cts$_{\rm h}$+Cts$_{\rm s}$), where "h" and "s" refer to the hard and soft bands, respectively. In absorbed regions, hardness ratios are of inherently limited value because of biases in the selection of bandpasses which lead to very non-uniform errors and a limited dynamic range. Sources with low counts tend to be driven toward the center of the distribution and there is a fundamental difficulty in breaking the degeneracy between temperature and absorption. To compare X-ray sources in the various regions of the cluster we use a quartile analysis technique for model-free analysis of X-ray data explored by Hong et al. (2004).

In this form of quartile analysis, one starts with the full ACIS band pass of $E_{\rm lo} = 0.3$ keV and $E_{\rm up} = 8.0$ keV. These are the same bandpasses that we used in our previous study of RCW 38 (Wolk et al. 2006). E_x is defined as the photon energy below which x% of the photon counts are found and $Q_x = (E_x - E_{\rm lo})/(E_{\rm up} - E_{\rm lo})$ is defined to be the normalized quartile.[7] In essence, the median compares the hard and soft portions of the spectrum. The ratio of the bottom to top quartile ($x = 25$ and 75, respectively) is representative of a two-point slope of the spectrum. For the case of a single temperature, the median energy is more sensitive to the absorption. However, quartiles are not independent, as the absorption changes the quartile ratio for a given temperature. Hong et al. plot the data by normalizing the quartile ratio axis as $3 \times Q_{25}/Q_{75}$ while the compressed median is expressed as $\log(m/(1-m))$, where m is the median. On such a plot one can distinguish changes in temperature from extinction and can even distinguish thermal and non-thermal changes.

Based on the colors of the sources as shown in Figure 2, it is clear that the center of the field has more embedded and/or hotter sources while the eastern field seems cooler and less embedded. We quantify this using the quartile values. These regions are defined as shown in Figure 5. The bulk of the sources are in the region east of R.A. 16:40:19, a second large region is west of R.A. 16:39:41. The final two areas are a region to the north of declination −48:48:34 and a regions south of declination −48:54:47. The latter two regions are chosen to exclude sources in the other regions. Thus the northern region is roughly coincident with the northern extension of the warm dust ridge. In Figure 6 quartile values of the sources in cardinal regions of the fields are compared.

The bulk of the sources to the east of the central region are associated with NGC 6193. Figure 5 shows a sharp increase in 8 μm emission along NGC 6188 which, at closest approach, is ∼1.2 pc from the central O star of RCW 108–IR (in the IRS 29 complex). Based on this, and the distinct change in the quartile values for data between ∼1.15 pc and ∼1.5 pc, the core region is defined to be within about 185″ of the central O star. The inner region is defined as a roughly square region ∼2.3 pc across so that all sources are included in one of the five regions. This is essentially coincident with RCW 108–IR, and will henceforth be referred to as such.

[7] Formally, Q_x is a "quantile"; however, the quantiles of 25, 50, and 75 percent are specifically known as "quartiles."

Table 5
Quartile Values of X-ray Sources

SRC #	$Q25$	$Q25_{err}$	M	M_{err}	$Q75$	$Q75_{err}$	$\log(m/(1-m))$	$3*Q25/Q75$
East								
1	0.147	0.012	0.228	0.019	0.399	0.031	−0.530	1.105
2	0.100	0.005	0.145	0.011	0.208	0.017	−0.771	1.442
3	0.086	0.009	0.131	0.010	0.188	0.027	−0.822	1.372
4	0.108	0.003	0.153	0.003	0.224	0.012	−0.743	1.446
5	0.100	0.014	0.141	0.015	0.176	0.048	−0.785	1.705
6	0.106	0.006	0.133	0.012	0.177	0.019	−0.814	1.797
7	0.102	0.009	0.146	0.008	0.213	0.021	−0.767	1.437
8	0.124	0.008	0.180	0.010	0.254	0.035	−0.659	1.465
9	0.095	0.007	0.130	0.014	0.199	0.025	−0.826	1.432
10	0.095	0.015	0.146	0.011	0.249	0.060	−0.767	1.145
11	0.080	0.007	0.101	0.008	0.137	0.071	−0.949	1.752
12	0.111	0.003	0.168	0.005	0.294	0.015	−0.695	1.133
13	0.111	0.012	0.144	0.023	0.273	0.118	−0.774	1.220
14	0.089	0.014	0.154	0.019	0.226	0.109	−0.740	1.181
15	0.029	0.012	0.068	0.048	0.240	0.134	−1.137	0.363

(This table is available in its entirety in a machine-readable format. A portion is shown here for guidance regarding its form and content)

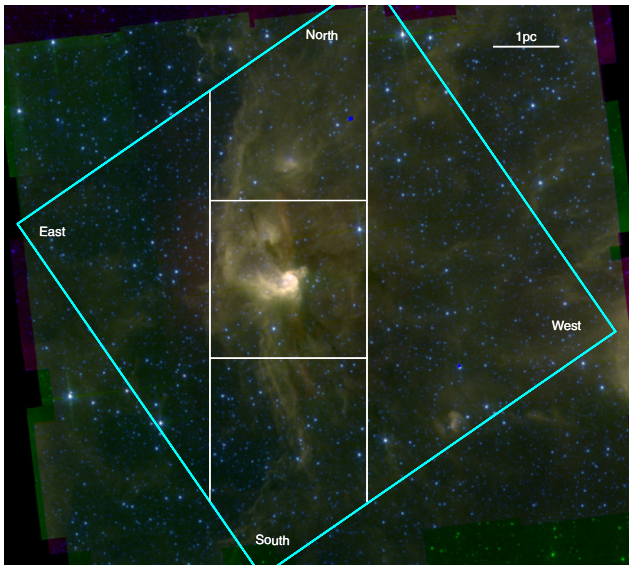

Figure 5. Definitions of regions overlain on the *Spitzer* image (BGR = 4.5 μm, 5.8 μm, and 8.0 μm, respectively) The *Chandra* field of view is indicated by the blue square. The eastern region is clearly part of NGC 6193. The northern region contains bright dust emission.

The values of $\log(m/(1-m))$ and $3 \times Q_{25}/Q_{75}$ are tabulated in Table 5 and shown in Figure 6. The errors for the quartile values are estimated using the method of Maritz & Jarett (1978) which has been found to reflect the results of simulations, including those of Hong (2004). Composite quartile values for each region are shown in Table 6. The difference between the central region and eastern region is very pronounced and indicates to a large statistical significance that these regions contain different kinds of sources or sources under difference circumstances. Comparing the sources among the other three cardinal directions indicate a similarity among them and that they are intermediate between those in the central region and those in the east.

These intermediate quartile values are indicative either of mixing or that these regions contain different evolutionary stages. In either event it is clear that the central region is not simply a foreground object over a background of younger sources stretching across a field. Further, it is noted by Wolk et al. (2007) that IRAS 16348–4849, which lies about 3.8 pc west of RCW108–IR, is connected to RCW108–IR by tendrils of warm dust, which are clear in the *MSX A*-band data (Figure 3). IRAS 16348–4849 has IRAS colors consistent with its being a star-forming region. Thus, X-ray sources in the south, north, and west could have IRAS 16348–4849 as their origin.

Table 6
Median Quartile Value by Region

Region	Number	$\log(m/(1-m))$	±	$3 \times Q_{25}/Q_{75}$	±
North	31	−0.58	0.09	1.02	0.07
South	41	−0.59	0.07	1.22	0.05
East	106	−0.77	0.01	1.23	0.04
West	63	−0.60	0.05	1.11	0.08
Inner 1′	31	−0.30	0.06	1.56	0.06
Annulus from 1′ to 3.5′	65	−0.30	0.04	1.34	0.05
Field	337	−0.67	0.27	1.32	0.33

3.4. Diffuse X-Ray Emission

Diffuse X-ray plasma has been previously observed in several regions of massive star formation (Townsley et al. 2003). It is thought that OB stars excavating an H II region may generate diffuse X-rays as fast winds shock the surrounding media (Weaver et al. 1977). *Chandra* observations have recently revealed parsec-scale diffuse emission in Galactic high-mass star-forming regions RCW 38 (Wolk et al. 2002), M17, and the Rosette Nebula (Townsley et al. 2003). This high-energy diffuse plasma plays a role in the evolution of the cluster by selectively clearing gas and dust.

To search for diffuse X-ray emission in the vicinity of RCW 108–IR, we selected six circular regions in zones without an X-ray source, within 35 arcsec of the cluster center (16:40:00, −48:51:40). The diameter of the zones varied from 8″ to 12″. The total area of these six regions is 510.5 arcsec^2. The CIAO tool *dmextract* was used to count the number of photons in the composite region. The total was 200 photons with a Gaussian error of photons in the composite region of 0.391 ±

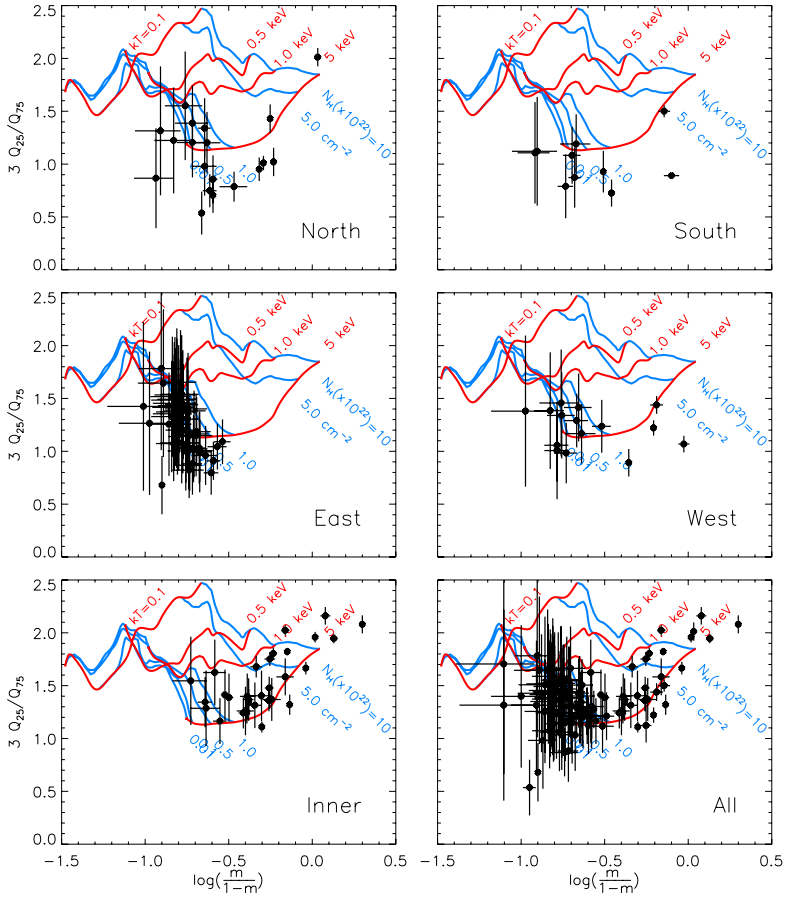

Figure 6. Quartile analysis of X-ray sources for the regions defined in Figure 5. region. The first four frames are the extreme 3′ to the west, north, east and south, respectively. The last two figures show the inner region and the whole field. In each frame, the Y axis is 3 Q_{25}/Q_{75}, the X-axis is the scaled median $\log(m/1-m)$, the blue lines indicate lines of constant hydrogen column, the red lines indicate lines of constant temperature. The data for the first four frames are statistically similar but distinct from the extreme central region (frame 5).

0.027 counts arcsec^{-2}. An annular background region was created centered on the cluster center with an inner radius of 148 arcsec and an outer radius of 408 arcsec for a total area of 4.36×10^5 arcsec^2 which was clearly not effected by diffuse emission. Counts were extracted from the region with sources removed. The background region contains $133\,465 \pm 365$ counts ($0.307 \pm 8 \times 10^{-4}$ counts arcsec^{-2}). This suggests a 30% excess of counts in RCW 108–IR which is about 2σ above the expected level. This is only about 20 counts, and can easily be accounted for by the >100 stars which are not detected in the X-ray data but should be present based on the detection of 35 X-ray sources in this highly absorbed region (see Section 4.3). We conclude that there is no significant diffuse plasma within this region. This is consistent with expectations discussed by Townsley et al. (2003) in which they concluded winds and mass loss consistent with an O6 star or earlier would be required to generate such a plasma, unless there had been a recent supernova. Here the central star has been determined to be O9.

4. SPECTRAL ANALYSIS

X-ray sources were fitted with spectroscopic models using *Sherpa* (Freeman et al. 2001). Background regions were generally selected as annuli around the source regions. Source and background pulse height distributions in the total band (0.3–8.0 keV) were constructed for each X-ray object. The final fits were done with CIAO version 3.3.0.1. The CIAO script *psextract* was used to extract source spectra and to create ancillary response function (ARF) and redistribution matrix function (RMF) files which compensate for local and temporal variations in the ACIS response. Background corrected data from each region were fitted with an absorbed one-temperature Raymond–Smith plasma (Raymond & Smith 1977). Such models were found by Wolk et al. (2006) to have the lowest residual χ^2/(degree of freedom) − 1 in a comparison of several available models.[8] The photoelectric absorption cross-sections ($\sigma(E)$) were taken from Morrison & McCammon (1983). Models were fitted both unbinned, using the C-statistic (Cash 1979) and binned using the data variance form of the χ^2 statistic (χ–DVAR). In the case of the binned data, data for each source were grouped into energy bins which required a minimum of 8 counts per bin and background subtracted. χ–DVAR is a statistic with variance computed from the data and is appropriate if the number of counts in each bin is large (>5) and the shape of the Poisson distribution from which the counts are sampled tends asymptotically toward that of a Gaussian distribution. For the binned and unbinned cases, the optimization method was set to Levenberg–Marquardt and Powell, respectively. Absorption

[8] Other spectral models including APEC (Smith et al. 2001) and mekal (Mewe, Gronenschild & van den Oord 1985) are available from the ANCHORS website: http://cxc.harvard.edu/ANCHORS.

Table 7
One-Temperature Spectral Fits

SRC #	χ^{2a} (per d.o.f.)	N_H (10^{22} cm^{-2})	N_H err (10^{22} cm^{-2})	kT (keV)	kT err (keV)	Abs. Flux	Unabs. Flux	Log L_x (erg s^{-1})
East								
1	0.62	0.55	0.15	5.51	1.87	−13.73	−13.53	30.77
2	0.58	0.44	0.08	1.10	0.08	−13.90	−13.40	30.91
3	0.53	0.79	0.09	0.61	0.07	−14.29	−13.28	31.03
4	0.47	0.17	0.03	2.65	0.31	−13.14	−12.95	31.36
5	0.29	1.03	0.18	0.56	0.11	−14.87	−13.63	30.67
6	0.51	0.34	0.12	1.14	0.13	−14.42	−13.99	30.31
7	0.37	0.09	0.06	2.34	0.54	−13.87	−13.72	30.58
8	0.38	0.40	0.10	2.52	0.54	−13.80	−13.52	30.79
9	0.39	0.58	0.12	0.95	0.15	−14.42	−13.78	30.53
10	0.35	0.04	...	2.93	1.13	−14.20	−14.12	30.19
11	0.25	0.01	...	1.02	0.18	−14.57	−14.48	29.83
12	0.56	0.20	0.04	4.01	0.54	−13.05	−12.89	31.41
13	0.39	0.73	0.16	0.82	0.15	−14.67	−13.86	30.45
14	0.37	0.01	...	2.04	0.84	−14.39	−14.34	29.97
15	0.29	0.02	...	0.09	0.01	−13.80	−13.11	31.20

Note.
[a] χ^2/d.o.f is included for completeness. These models were calculated with C statistics; it is unclear how χ^2/d.o.f relates to goodness of fit. The formal errors are unbiased; however, see the text.
(This table is available in its entirety in a machine-readable format. A portion is shown here for guidance regarding its form and content)

and temperature were simultaneously fitted for each observation and the resultant 95% emergent flux was calculated and then scaled to 100%. Formal flux errors are about 4% at 2,000 counts, about 35% at 100 counts, and errors reach 100% below about 30 counts. Formal errors underestimate the real uncertainty as demonstrated by the variance in the temperatures and hydrogen columns measured using difference techniques. This variance can exceed the formal errors by about 50%.

Two advantages of the C-statistic method are that the data are unbinned and thus sources with a small number of counts may be fitted and the errors are symmetric and so should not affect an ensemble analysis of the dataset. A drawback is that the goodness-of-fit information suffers when unbinned data are used (Heinrich 2003). In the end, we generally used unbinned C-statistics for the sources with over 3.5 "σ" significance. In a few cases, the temperatures found using C-statistics was above 15 keV while χ–DVAR temperatures were more reasonable, below 7 keV. In other cases C-statistic fits were indeterminate in N_H. In these cases, again the χ–DVAR results were used. The result of the single-temperature fits using C-statistics are listed in Table 7. Column 1 gives the source name from Table 1, Column 2 gives the goodness-of-fit to an absorbed one-temperature Raymond–Smith plasma in terms of χ^2/degree of freedom (but note the caveat above). Columns 3–7 give the fit parameters N_H, kT, associated errors and the log of the unabsorbed flux. The luminosity of each source is calculated based on the derived unabsorbed flux and the cluster distance of 1.3 kpc and listed in Column 8. Fluxes and luminosities are corrected for the 95% encircled energy radius. The sources in Table 7 are subdivided by their region as described in Section 3.3.

Two issues are present throughout the fitting process. First, there is a fundamental degeneracy in the fits between N_H and kT. It is possible that fits of similar quality can be obtained by increasing N_H and an appropriate increase in the temperature. While this is especially true in regions of high absorption such as the core region RCW 108–IR the temperature range in question is typically about 2 keV. Temperatures between 3 and 8 keV or less than 1 keV are very robust given enough data. Second, since there is little sensitivity to X-rays above 10 keV, model fits are not very reliable much above this energy range. Because of this, if the fitted temperatures exceed 15 keV we simply label them "$>$15" in the tables.

4.1. Two-Temperature Fits

In many cases of stars with high flux rates, a second thermal component is clearly needed to fit a deficiency in the temperature model seen at low energies. In addition to the single temperature fits, absorbed two-temperature fits were made for 73 sources with over 100 net counts. Of these, only 54 were considered true two-temperature fits with temperatures different by more than 10% and each component contributing at least 10% of the flux. Twenty-two of these were rejected for having poor formal constraints on the temperatures (formal errors exceeding 10 keV). The absorbed two-temperature fit was deemed superior to the one-temperature fit for 22 X-ray sources (Table 8). The first six columns of Table 8 are identical to those of Table 7. Columns 7 and 8 are the high-temperature component. Columns 9–11 are the log of the absorbed and modeled unabsorbed fluxes. Columns 12 and 13 list the log of the emission measure for the cooler and warmer components, respectively, and Column 14 gives log of the luminosity. Again, the sources are subdivided by their region as described in Section 3.3.

The results of the two temperature fits show that given sufficient flux, about one third of the sources are better represented as two-temperature models. The key datum from these fits is that the global extinction is much better constrained. The eastern sample is large enough (14) to look at the group statistically. To the east $\langle N_H \rangle = 0.42 \pm 0.24 \times 10^{22}$ cm^{-2}, while in the center $N_H > 2.4 \times 10^{22}$ cm^{-2}. Also interesting is that the cool components are about 700 eV ($\pm$30 eV), while the warmer components are about 2.45 keV ($\pm$1.07 keV). This indicates much more variability in the temperature of the hot component than the cool component. In the case of the cool component, this

Table 8
Sources with Two-Temperature Spectra

SRC #	χ^{2a} (per d.o.f.)	N_H (10^{22} cm^{-2})	N_H err	kT_1 (keV)	kT_1 err	kT_2 (keV)	kT_2 err	Abs. Flux (erg cm^{-2})	Unabs. $Flux_1$ (erg cm^{-2})	Unabs. $Flux_2$ (erg cm^{-2})	EM_1 log (cm^{-6})	EM_2 log (cm^{-6})	L_x log (ergs^{-1})
East													
2	1.07	0.47	0.09	0.86	0.13	2.09	0.77	−13.86	−13.77	−13.69	53.02	53.51	30.88
4	0.95	0.25	0.04	0.75	0.14	2.67	0.41	−13.18	−13.90	−12.99	52.85	54.18	31.37
7	0.88	0.51	0.10	0.54	0.27	2.33	0.70	−13.92	−13.84	−13.69	52.78	53.47	30.85
12	0.95	0.35	0.04	0.86	0.10	5.30	1.83	−13.06	−13.53	−12.95	53.29	54.11	31.46
30	0.38	0.48	0.07	0.70	0.11	2.72	0.96	−13.77	−13.55	−13.68	53.67	53.48	31.00
230	0.96	0.59	0.05	0.14	0.01	0.98	0.08	−13.55	−12.05	−13.02	54.83	54.18	32.30
233	1.80	0.44	0.08	0.21	0.04	1.07	0.12	−13.94	−13.31	−13.56	53.91	53.39	31.19
245	0.99	0.21	0.03	1.00	0.07	2.96	0.33	−12.78	−13.33	−12.65	53.57	54.51	31.74
248	1.16	0.07	0.07	0.92	0.26	1.96	0.70	−13.77	−14.37	−13.70	52.45	53.51	30.69
255	0.73	0.10	0.05	1.05	0.09	3.55	0.93	−13.33	−13.87	−13.29	53.06	53.83	31.12
257	0.64	0.28	0.04	0.86	0.09	2.41	0.42	−13.32	−13.61	−13.17	53.21	54.01	31.27
North													
134	0.39	0.95	0.13	0.44	0.11	2.67	0.73	−13.79	−13.39	−13.47	53.48	53.70	31.18
262	1.09	0.24	0.07	1.21	0.43	2.94	1.00	−13.50	−13.94	−13.38	53.08	53.77	31.03
RCW 108–IR													
116	1.06	2.45	0.21	1.21	0.43	2.80	0.47	−13.36	−13.09	−12.96	53.91	54.20	31.58
118	0.90	3.48	0.12	0.57	0.08	2.61	0.13	−12.63	−11.88	−12.06	54.82	55.11	32.65
136	0.84	1.15	0.10	0.71	0.15	2.42	0.55	−13.15	−12.68	−12.82	54.41	54.32	31.86
South													
64	0.74	1.58	0.11	0.69	0.09	2.72	0.82	−13.60	−12.66	−13.37	54.06	53.78	31.73
267	0.78	0.01	0.06	0.44	0.11	1.16	0.32	−13.97	−14.15	−14.23	53.01	52.77	30.42
West													
158	1.01	0.37	0.08	0.23	0.06	0.90	0.12	−14.18	−13.81	−13.76	53.12	53.43	30.82
164	1.22	0.19	0.08	0.89	0.14	2.15	0.96	−13.90	−14.07	−13.84	52.77	53.37	30.67
170	1.02	0.80	0.14	0.76	0.33	3.60	1.16	−13.67	−13.93	−13.42	52.84	53.70	31.01

Note. [a] Data variance χ^2/d.o.f. statistic has a mean of 1 for a good fit.

result is consistent with earlier X-ray studies of young stars which show a stable ∼800 eV corona distinct from the high temperature corona (Sanz-Forcada et al. 2003). The difference in the high-temperature component may be indicative that the sources to the west are younger than those to the east. The high-temperature component in the X-ray sources to the north and south are more consistent with those in the east. The temperatures of the cool coronae in the core region are harder to evaluate due to the higher absorption present there, the high-temperature components are similar to those in the west. The variability in the high temperature component may also be indicative of different levels of flaring. As will be shown in Section 5.1, several of these sources flared.

4.2. Temperature and Hydrogen Column Density Distribution

Because so few sources were well characterized by two-temperature spectra, we used the one-temperature fits to analyze the overall nature of the sources. We confined the analysis to high-quality data as described below. Since formal goodness-of-fit is inappropriate for the C-statistic, the quality of the fits is evaluated using three metrics. First the net counts need to exceed 50 so that a meaningful fit is possible. The second and third metrics are the ratio of the formal errors to the measured values N_H and kT. These act as a statement on the quality of the measurements and limits the effect of errors in the evaluation of global properties. Overall, about 90 spectra have errors of less than 50% in N_H and kT. The mean N_H of these ∼90 sources is 5.3×10^{21} cm^{-2}. But almost 25% of the sources were rejected from this calculation because they were more than 3σ from the mean. This indicates a very non-Gaussian distribution of sources, as expected from the quartile analysis. To study the changes in the spectral characteristics of the X-rays sources spatially across the field we divided the regions described in Section 3.3.

Table 9
X-ray Spectral Properties by Region

Region	Number	kT (keV)	MAD	Rejected	N_H ($\times 10^{22}$ cm^{-2})	MAD	Rejected
North	7	2.78	0.49	0	0.54	0.09	0
South	12	2.79	0.66	0	0.69	0.10	1
East	29	1.44	0.15	3	0.41	0.04	1
West	20	2.87	0.39	0	0.53	0.06	3
RCW 108–IR	21	3.07	0.29	0	2.29	0.28	2
Field	89	2.54	0.17	0	0.53	0.04	20

A global comparison of the spectral fits for the sources in the regions is summarized in Table 9. In this Table, restricted to bright sources with over 50 counts and formal errors in kT and N_H of <50%, Column 1 indicates the source region, Column 2 indicates the number of qualifying sources in the region. Columns 3–5 list the mean kT, median absolute deviation (MAD; Beers 1990)[9] and the number of 3σ outliers in each region. Columns 6–8 list the mean N_H, MAD and the number of 3σ outliers. This spectroscopic summary confirms the evidence given by the quartile analysis that the five regions contain at least three types of sources: hot and embedded in the center,

[9] The median absolute deviation is the average deviation from the median measured as absolute values. It is an outlier-resistant measure of the variability, making it useful for describing the variability of data with outliers. It is a common measure of forecast error in time series analysis.

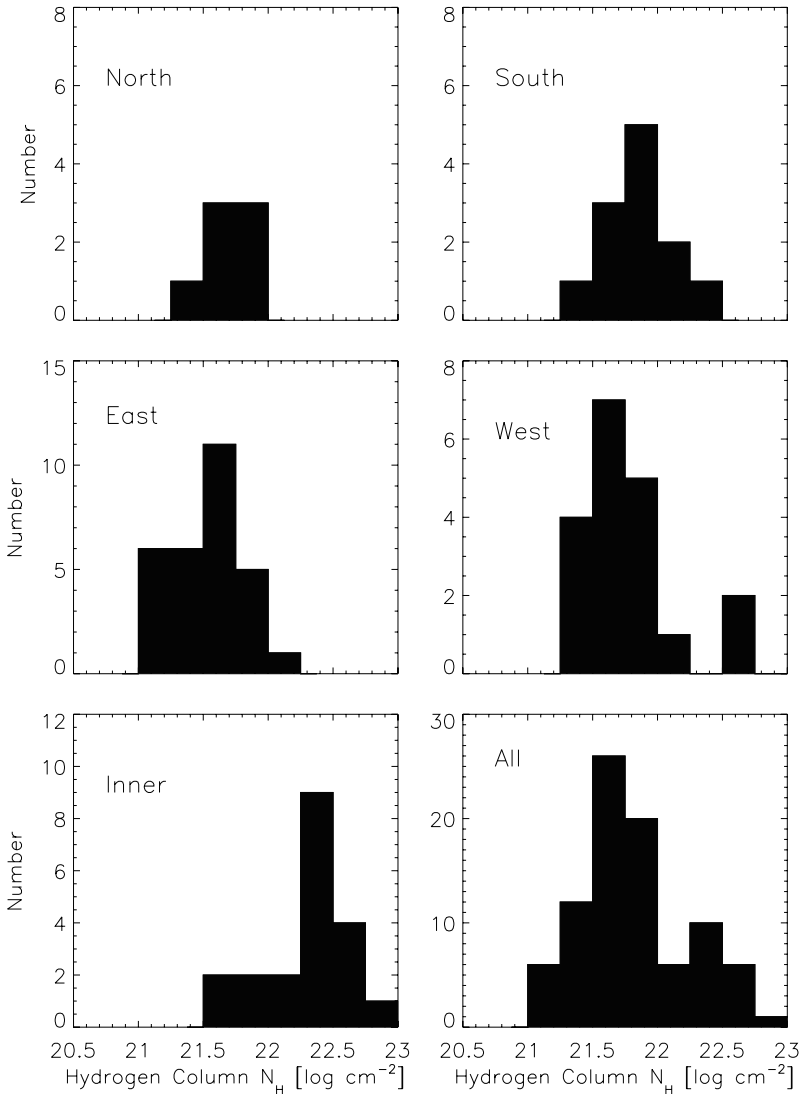

Figure 7. Histograms of hydrogen absorption column, $N_{\rm H}$, derived through spectral fits of X-ray sources with over 50 counts and formal errors $< 50\%$. The bin size is 0.25 dex. The six panels are marked to indicate the location of the X-ray sources with respect to the field of view, see Figure 6 for details.

cool and low extinction to the east, while the other three regions are intermediate. We note that while thermally the three intermediate regions are ordered west, south and north (hottest to coolest) the hydrogen columns are ordered south, north, and west (highest to lowest). The differences among the hydrogen columns in the south and west regions are statistically insignificant.

These results are displayed schematically in Figures 7 and 8. In these figures, the results are broken down region by region using histograms. From Figure 7 it is clear that there are no bright X-ray sources with column densities $<10^{21}$cm^{-2} in the entire field. This means that there is little foreground contamination among the bright sources. The distinction between RCW 108–IR and eastern region is clear with moderate overlap in log($N_{\rm H}$) between 21.5 and 22 cm^{-2}. Columns densities to the north are completely consistent with those in the east, while the southern and western regions possess some more absorbed sources. Figure 8 again shows that the sources in RCW 108–IR and eastern regions form fairly distinct groups. There are a few very hard sources in the eastern region. Overall, there are eight high-quality sources with measured temperatures in excess of 5 keV ($\sim$50 MK); three of these are in RCW 108–IR , two are to the south and one each are in the eastern and western regions. While the sources in the central region tend to be more absorbed and hotter, region-by-region analysis shows there is no strong correlation between $N_{\rm H}$ and kT.

4.3. X-Ray Luminosities

As clusters age, the luminosity of their members will drop at different rates for stars of different masses and this will be reflected in the cumulative distribution of X-ray luminosities—the X-ray luminosity function (XLF). Feigelson et al. (2005) have attempted to understand the X-ray luminosity function as a global property of star-forming regions. For regions at very young ages, similar to that of NGC 1333 or the Orion Nebular Cluster (ONC), they find that when high-mass stars are excluded, the XLF follows a somewhat flattened lognormal distribution with a mean of log $L_X \approx 29.3$ and a standard deviation of ± 1.0. Our analysis of the XLF of RCW 38 was consistent with this lognormal distribution (Wolk et al. 2006).

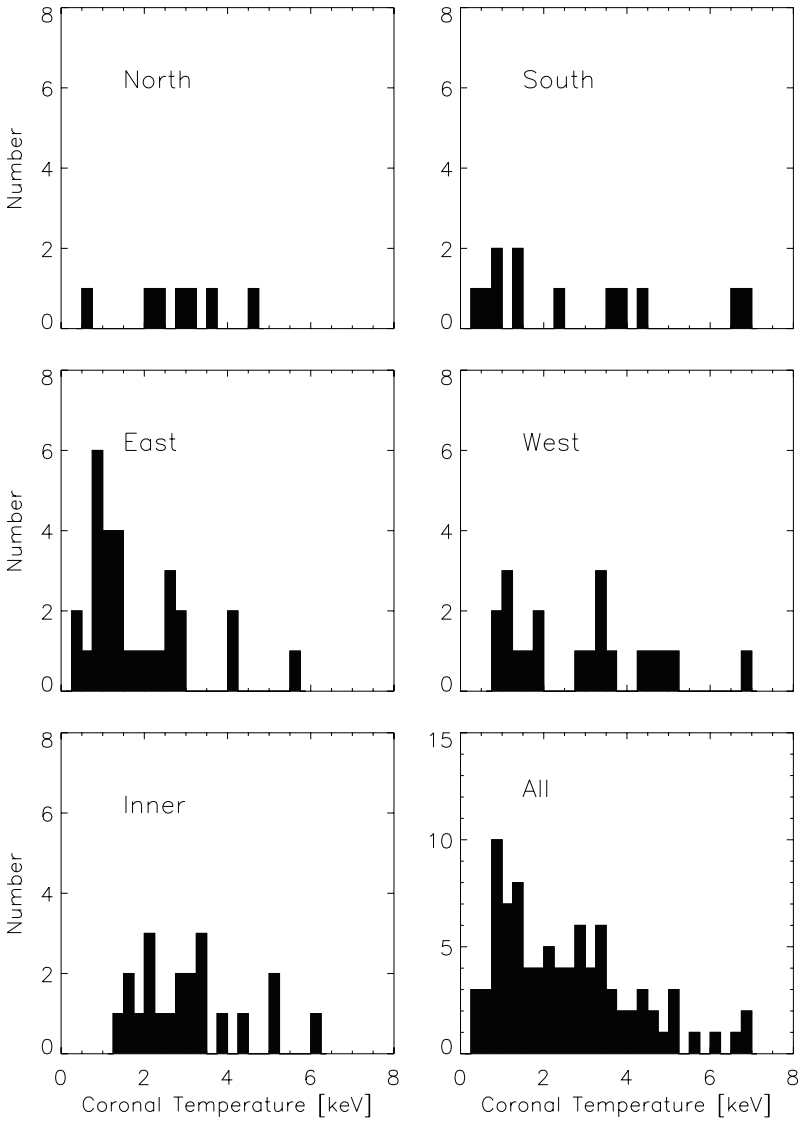

Figure 8. Histograms of coronal temperature, kT, derived through single temperature spectral fits of X-ray sources with over 50 counts and formal errors < 50%. The bin size is 0.25 keV. The six panels are marked to indicate the location of the X-ray sources with respect to the field of view; see Figure 6 for details.

We calculate luminosities for each source using the fluxes and line-of-sight absorptions, determined from the C-statistic fits and assuming a distance of 1.3 kpc. While we do not explicitly exclude high-mass stars as done by Feigelson et al. (2005), we expect them to be few in number relative to the low-mass stars and to have a negligible impact which is uniform across all luminosity bins, as seen by Feigelson et al. (2005). Below about 50 counts, the individual estimates have errors exceeding a factor of 2. This is mostly due to the poor determination of $N_{\rm H}$. There is no evidence that such errors are markedly biased by the C-statistic and thus the XLF derived using data with such low counts is still valid. We do not include the 87 faintest sources in this analysis since luminosities were not calculated for them.

In Figure 9 the XLFs of the five regions and the whole field are shown. On the left-hand plot the cumulative totals are shown, region by region. The dotted line shows the cumulative total of a lognormal distribution along with observed distribution. The cumulative total of a lognormal distribution has been scaled to equal the observed data in the bin where $\log(L_X) = 30.5$. We expect the data to complete in this bin and the adjacent bins (see below), thus lognormal distribution indicates what would be observed in an observation that was sensitive to all low luminosity sources. Fitting the observed and complete portion of the XLF with the "global" XLF offers the intriguing possibility of estimating the total cluster size and/or distance. Since the distance to this cluster is not in dispute (±10%) we can estimate the total number cluster members in the field at about 1600 ± 200, with about 800 ± 100 in the central region.

Such extrapolations become very uncertain due to completeness issues. Feigelson et al. (2005) provide a rough estimate of the *Chandra* sensitivity as

$$\log\ L_x = 28.7 + 2\log(d/\mathrm{kpc}) - \log(t_{\rm exp}/100\ \mathrm{ks}) + 0.4(\log\ N_{\rm H} - 20)\ \mathrm{erg\ s^{-1}}. \quad (2)$$

Assuming a distance of 1.3 kpc and estimating $\log\ N_{\rm H} = 21.5\ \mathrm{cm^{-2}}$ in most of the field, we derive a sensitivity limit

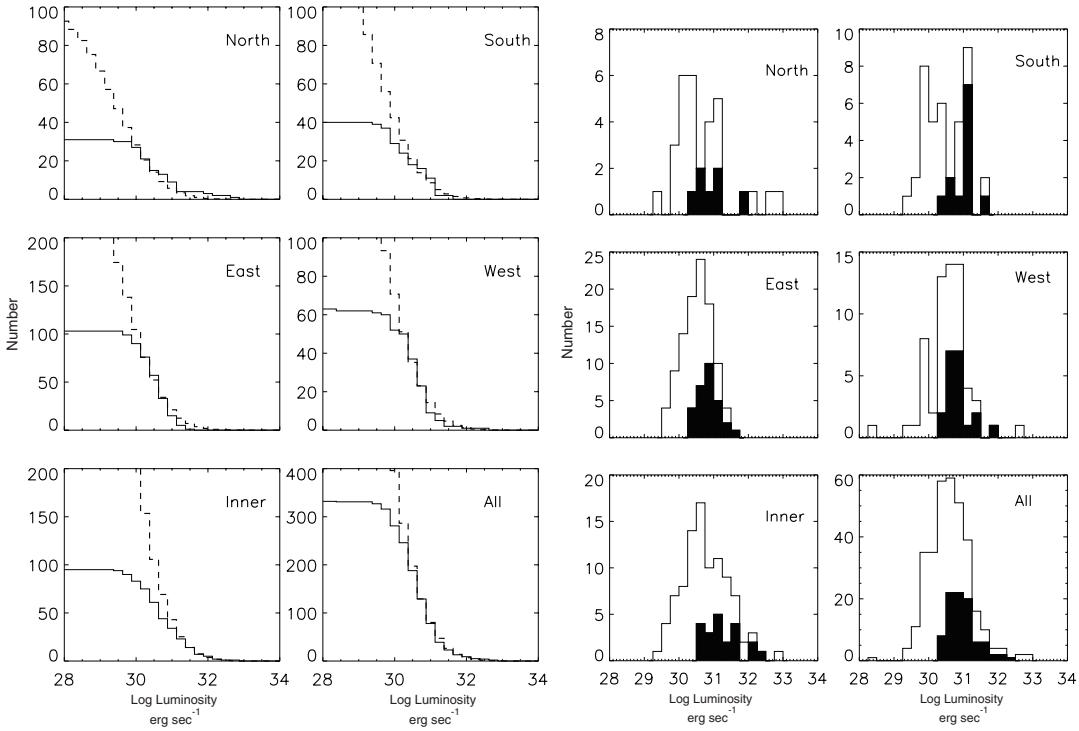

Figure 9. X-ray luminosity distributions segregated by region. Left: The cumulative distribution for each region is shown as the solid histogram. The dotted histogram is from a lognormal function normalized to equal the observed distribution at log $L_x \sim 30.5$ (31 for the inner region). Right: a non-cumulative distribution of the observed luminosities. The solid histogram indicates the luminosity distribution of bright sources with low errors in kT and $N_{\rm H}$. This figure emphasizes deviations from a Gaussian profile of the XLF in the north and the south.

of about log $L_x = 29.6\,{\rm erg\,s^{-1}}$ in the bulk of the field and log $L_x = 29.8\,{\rm erg\,s^{-1}}$ or so in the core where we assume log $N_{\rm H} \sim 22\,{\rm cm^{-2}}$. This latter value is clearly too small since we only estimate the absorption to the sources that we detect. The true mean absorption to the core region is much higher, perhaps as high as 23.5 in log based on the IR data. This is reflected in the cutoff in the luminosity function near log $(L_x) \approx 30.5$. The luminosity is corrected for spotty absorption and we can estimate completeness based on the location of the break in the observed XLF from the log normal form. This lack of precision in this completeness estimate leads to the error estimates given above.

The eastern region lacks the high-luminosity tail. Our sample of the XLF is taken from the southern portion of NGC 6193 and appear to be "missing" sources as the high luminosity/high mass end. This implies that the sample is depleted in early G stars, relative to K stars. Since we are not sampling the central region of NGC 6193, and only the southwestern portion, it appears that mass segregation has kept the most luminous members toward the center of the cluster outside of the field of view or moved the low-luminosity sources away from the cluster center and into the field of view. Thus, we obtain an incomplete view of this cluster. This inference is supported by the X-ray observations of the core of NGC 6193 that were made as part of the HETG observation of the HD 150135/6 O star pair at the center of NGC 6193. Skinner et al. (2005) report 43 X-ray point sources of which at least five are identified with OB counterparts. This is as many OB stars as we identify with over 100 X-ray sources in the southwestern portion of NGC 6193. Further, the earlier Chandra observation is only about 15% as deep as the observation we analyze here, so a smaller fraction of B stars was detected by Skinner et al. (2005).

The XLF in the west seems to also be biased away from high-luminosity sources though the limited number of stars in the region makes the determination difficult. The XLFs in the north and south regions are increasingly more poorly described by a lognormal. This is indicative that X-ray selection is incomplete for these sparse populations.

5. X-RAY VARIABILITY

In this section, we examine the variability of the X-ray source population. Variability studies allow us to begin to assess the plausibility of X-ray generation mechanisms. These can be constrained by the timescales and flux changes observed in the variability. Variability also offers corroborating evidence that a source is stellar in nature and hence a possible cluster member. Unlike other X-ray sources almost all coronal sources vary given a long enough observation (see Getman et al. 2005). These variations can either be stochastic or impulsive deviations from a constant rate.

Various methods can be employed to investigate variability. This topic has been reviewed briefly by Wolk et al. (2005) and more thoroughly by Güdel (2004) and Favata & Micela (2003). One rigorous technique commonly used is a one-sample Kolmogorov–Smirnov (KS) test to identify if the photon arrival times are consistent with a constant rate. The KS test does not give any information on the nature of the variability in objects. Thus we prefer the use of Bayesian Blocks (BBs; Scargle 1998). Bayesian Blocks not only detect variability, but provide a method of flare detection without the biases inherent in binning the data.

These techniques are discussed in some detail by Wolk et al. (2005, 2006), so we do not repeat the discussion here. We tested each lightcurve with a "prior ratios" set to approximate

both 95% and 99% confidence that a flux change had occurred. Overall 61 sources on the I array required more than one BB at greater than 95% confidence. We also tested the Gregory & Loredo (1992) method. This method uses maximum-likelihood statistics and evaluates a large number of possible break points from the prediction of constancy. The number of sources found to vary at a given confidence level agreed with the Scargle method, which is still our method of choice. The variability results using BBs are tabulated in column 8 of Table 1 which lists the number of BBs for each source. A number greater than one indicates that the source varied at the 95% confidence level during the observation.

5.1. Flaring

Amongst the brightest 30 sources (those with over 200 total counts), 20 (66%) were variable at >95% confidence. The variability rate drops among the 56 sources with between 100 and 200 net counts, of which 12 (21%) were variable at >95% confidence. Overall, 41% of the bright sources are detected as variable in 88.8 ks. The BB method converts the lightcurve to temporal periods of constant flux, thus, one can measure the amount of rise between the blocks and estimate the rate of change between blocks. In their study of the extremely deep COUP data set, Wolk et al. (2005) found that most stellar sources have a characteristic rate, $R_{\rm char}$ and found sources were at their characteristic levels for about 75% of the time. They further found that a normalized rate of rise,

$$\Delta \equiv 1/R_{\rm char} \times {\rm d}R/{\rm d}t > 10^{-4}{\rm s}^{-1}, \quad (3)$$

was indicative of a flare. Following Wolk et al. (2005) we define dR as the difference between the rates of adjacent blocks and dt as the shorter of the two blocks. We choose the value of the minimum block as the characteristic rate since we do not have the long observation time to define a true characteristic level. We also require the latter period to have a higher count rate, although the opposite may be indicative of a post flare decline. Twenty-eight sources have this form of impulsive variability (see Figure 10). No star was seen to flare twice. Thirty-four other stars were detected as variables (with 95% confidence) but were not seen to flare.

5.2. Flare Rates

These data can be used to assess flare rates. We constrain the following analysis to sources with over 100 counts to prevent biases since we are less sensitive to flares in stars with low counts. Thirteen of 72 (18%) probable cluster members with over 100 counts flared in ≈90 ks. Assuming that all stars are the same and that there are no stars more prone to flare than others then we conclude there are about 510 ks between flares. This is similar the values obtained for solar mass stars in the ONC (one flare per 640 ks; Wolk et al. 2005) and the very young and embedded cluster RCW 38 (one flare per 775 ks; Wolk et al. 2006).

A 100 Myr cluster, NGC 2516, was studied using a similar method and found to have a somewhat lower flare rate, about 1 per megasecond (Wolk et al. 2004). The flare rate might also be lower due to a sampling bias present in the NGC 2516 study—the lack of a low count limit. Indeed, when we calculate a flare rate base on 28 flares observed on 337 stars in the full RCW 108 field, the composite flare rate seen is about 1 per 1.11 megasecond. A similar pattern was recently found by Caramazza et al. (2007) when examining low mass (K & M) stars in the COUP field—flare frequencies are lower in low count rate samples. This occurs because the sensitivity to flares depends on source statistics. When examining low mass stars with between 100 and 200 counts, Caramazza et al. find a flare frequency of about 1/680 ks—very close to the rate we find at similar count rates in the full RCW 108 field. The COUP rate is about 1/800 ks below 100 counts. This is somewhat higher than the 1 per 1100 ks reported here. But the data presented here have not been filtered to exclude high-mass stars and background objects.

6. INFRARED PROPERTIES OF X-RAY SOURCES

Near-infrared (NIR) data were taken from three sources, the 2MASS catalog, NTT/SOFI observation of Comerón et al. (2005) and VLT/NACO adaptive optics data over the very central region of RCW 108–IR (Comerón & Schneider 2007). The latter data indicate NIR counterparts to five additional X-ray sources and show that at least three X-ray sources are associated with NIR pairs. These data are very recent and included solely for completeness. The NTT/SOFI data cover a 13′× 13′ (∼5 pc) field centered on RCW 108–IR with a somewhat deeper exposure for the central 5′(∼1.9 pc). The observation and reduction of these data are discussed by Comerón et al. (2005). Each X-ray source was matched to the nearest counterpart in each list. Matches were accepted if the offset between the X-ray and IR sources fell within the following empirically determined curve:

$$\text{offset} < 0.0003\theta^{1.55} + 1'', \quad (4)$$

where "offset" is the distance in arcseconds between the X-ray and NIR position and θ is the off-axis distance of the X-ray source, also in arcseconds. This curves allows offset of about 1″ on-axis. We impose a hard limit of 2.5″offset toward the edge of the field.

Once good matches were determined for each catalog the NIR catalogs were merged. When NIR counterparts were well observed by both primary input sources astrometry was taken from the global 2MASS program and photometry was taken from the deeper study by Comerón et al. (2005) which lacks high-precision astrometry. NIR counterparts were detected for 303 of the 337 brighter X-ray sources on the imaging array (about 90%). Among the additional 87 faint sources listed in Table 2, 56 (65%) had matches in either the 2MASS or Comerón et al. catalogs. This gives confidence to the veracity of the detected faint sources. The lower NIR detection of the faint sources has multiple origins. First of all, the likelihood of false X-ray detections is certainly higher. Within 4′, 6 counts is a clear detection at the three-sigma level. However, as θ becomes higher the area and the background count level increases, hence more counts are required for a detection. The matching radius also goes up so the possibility of a false match increases. If the IR sources are spread uniformly over the field, then the area available for matching goes as the square of the offset in Equation (4). Thus, the chance of random coincidence goes up nearly tenfold as θ increases from 60″ to 240″. This is mitigated by the fact that the NIR and X-ray sources *are* centrally condensed. Secondly, since the X-ray luminosity loosely follows the bolometric luminosity, the NIR counterparts of faint X-ray sources also become fainter. The mean *J* magnitude of the X-ray faint group is 15.8 while the mean *J* magnitude of the nominal X-ray group is 14.4. This is especially a concern in the 40% of the X-ray field not within the NTT/SOFI field of view since the 2MASS data have a brighter limiting magnitude. Finally, as

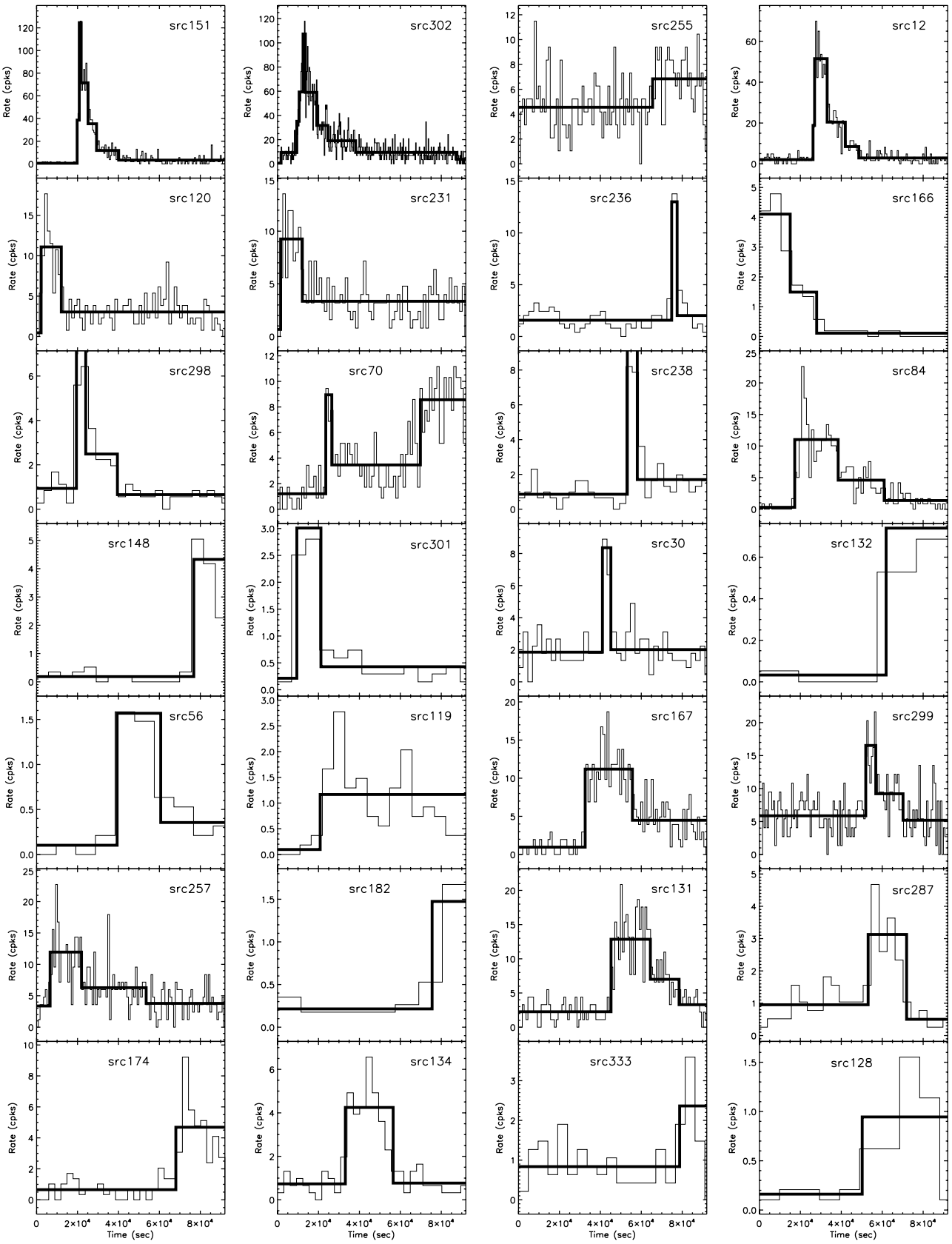

Figure 10. The 28 sources seen to flare. The lightcurves are plotted with an average of 5 (raw) counts per bin with the Bayesian blocks (95% confidence) overplotted as the thick line. Sources are ordered by the metric for flare intensity, Δ (see text), decreasing across and then down.

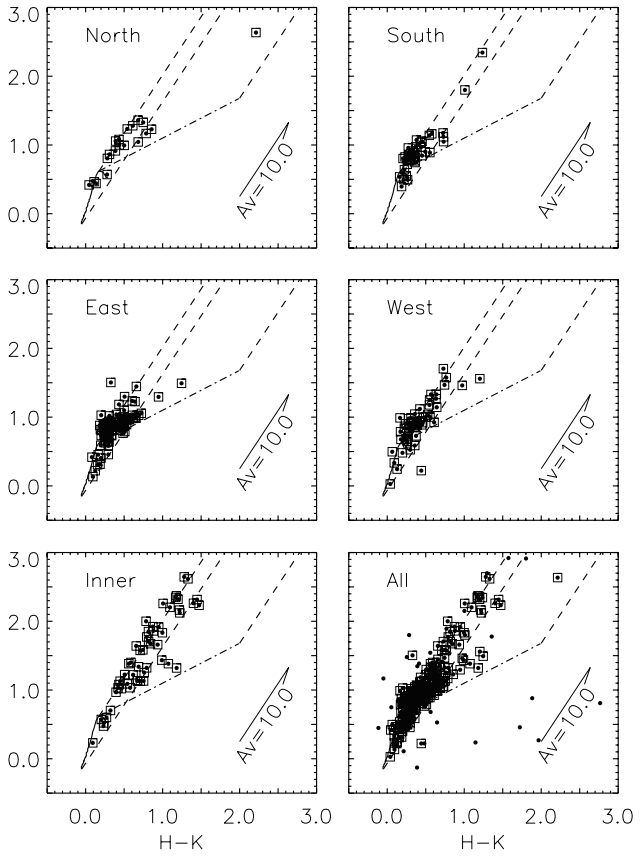

Figure 11. Infrared color–color diagrams ($J-H$ versus $H-K$) for counterparts to all X-ray sources in the RCW 108 *Chandra* field. For each panel, the solid line indicates the main sequence, the dashed line runs parallel to the reddening vector, and the dot-dashed line is the cTTs locus (after Lada & Adams 1992 and Meyer et al. 1997). A reddening vector indicative of $A_V = 10$ is marked. Sources marked as points have errors < 0.25 magnitudes. Sources marked also with squares have errors of <0.10 magnitudes at K_s. The six panels are marked to indicate the location of the X-ray sources with respect to the field of view; see Figure 6 for details.

the fluxes get fainter, detection of background objects such as active galactic nuclei (AGNs) becomes more likely.

The NIR data for all X-ray sources are tabulated in Table 10. In this table, Column 1 is the X-ray source ID, Columns 2 and 3 are the R.A. and decl. of the NIR source, Columns 4 and 5 are the offset between the X-ray and NIR position and the off-axis distance, respectively. Column 6–11 are the J, H, and K_s band magnitudes and errors. For photometry taken from 2MASS the last column carries the 2MASS quality flags; otherwise, if the photometry is taken from the NTT or VLT data the notation "NTT" or "VLT" is used. Table 10 is broken up into the five cardinal regions.

These data are used in Figure 11, which shows NIR color–color diagrams for each of the regions. RCW 108–IR has the highest extinction, with some sources exceeding A_V of 20. The western region also shows significant extinction with A_V approaching 8. The other four regions have more mild extinction but contain a few stars with anomalously high extinction seeming to indicate that they may be members of RCW 108–IR. We also note the lack of background giants; these are usually indicated by highly absorbed sources that lie just above the upper track of the reddening box, which is set for normal dwarfs and not giant stars. The only region that shows such sources is RCW 108–IR and we conclude such sources as certainly associated with the active star formation in RCW 108–IR. In the remaining fields there are few background giant candidates among the X-ray sources.

The IR color–color diagram provides global information about reddening, but does not provide much insight about the masses of the various sources. To get a sense of the masses of the stars in the field we use the IR color–magnitude diagram shown in Figure 12. This figure uses isochrones from Siess et al. (2000; SDF) set at 1.0 Myr and the zero-age main sequence (ZAMS) for reference only. The dashed lines indicate 20 magnitudes of visual extinction. The stars to the east are very tightly confined and most are consistent with little extinction. These stars range in mass but the bulk appear below the 2.5 $M_\odot$ line. Stars in the north, south, and west are more scattered. RCW 108–IR shows a near-perfect anti-correlation with the east. RCW 108–IR also shows a large number of sources with masses above 2.5 $M_\odot$. Either the stars in this region have a very different mass function, or we are only seeing the most massive sources due to extinction.

Following Comerón et al. (2005), we can assess the amount of infrared excess using the reddening free quantity:

$$Q = (J - H) - 1.70 \times (H - K_s). \quad (5)$$

Column 12 of Table 10 lists Q for each source. Values of $Q < -0.10$ are indicative of an infrared excess consistent with a disk. Overall about 33 of the over 330 X-ray sources with good infrared colors ($\approx$10%) have $Q < -0.10$. There are about 55 sources with $Q < -0.10$ and no X-ray detection. There is some field-to-field variation. In RCW 108–IR the fraction is somewhat higher, 13 out of 81 (16%). The eastern and southern regions have the lowest fraction of low Q sources at about 6%. The fractions in the west and north are 10% and 13%, respectively. From all of these assessments, it would appear that a relatively small fraction of sources have disks which are optically thick at K_s. These results are consistent with Comerón et al. who found 87 such sources among over 4300 in the central field. However Q cannot distinguish among stars with less extreme optically thick disks. For this, mid-IR data are useful.

6.1. Mid-Infrared Properties of X-ray Sources

For each source in the *Chandra* source list, the nearest IRAC counterpart was identified. For X-ray sources with off-axis angle (θ) less than 200″, the maximum X-ray/IR offset allowed was 1″. For off-axis angles between 200″ and 600″, the maximum offset was 2.5″. Overall, 236 X-ray sources were matched to the IRAC source list which included about 2600 detections. Of the 236 counterparts, 33 of these are associated with stars with normal photospheres, while there are 58 Class II objects and five Class I objects. Two are identified as probable galaxies. The remaining 140 sources are of unknown type due to incomplete data in the IRAC channels. Many of these sources only have detections in one or two bands.

The infrared characteristics of the X-ray sources are listed in Table 11. The IRAC Class I sources are particularly intriguing as they should identify sites of the most active star formation. The key color for the determination of Class I sources via IRAC is the [4.5]–[5.8] color (>0.5) with [3.6]–[4.5] color being used as a secondary indicator. This is shown in the bottom of Figure 13. The color cutoffs are determined empirically from low mass young stellar objects (Gutermuth et al. 2007). The Class I sources are clear as outliers in H-4.5 μm color (top of

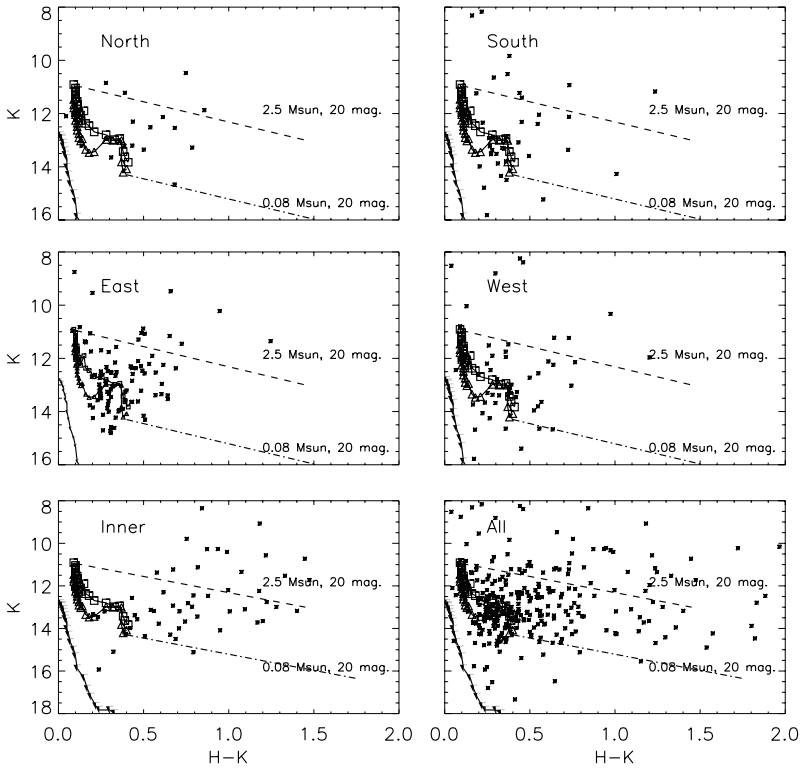

Figure 12. Infrared color–magnitude diagrams (K_s versus $H - K_s$) for counterparts to all X-ray sources in the RCW 108 *Chandra* field. For each panel, the 0.5 Myr (open squares), 1.0 Myr (open triangles), and ZAMS (filled circles) isochrones for 2.5 $M_\odot$–0.08 $M_\odot$ are plotted (Siess et al. 2000). Extinction of 20 visual magnitudes for a 2.5 $M_\odot$ star indicated by the dashed lines. The dot-dashed lines indicate 20 visual magnitudes for 0.08 $M_\odot$ stars at ages of 0.5 Myr. High-mass stars are predominately seen in the inner region.

Table 10
Near-IR Observations of X-Ray Sources

SRC #	IR R.A.	IR Decl.	Offset	Off-axis	J	Jerr	H	Herr	K	Kerr	Q	A_V	Model	Flags
East														
1	16:40:36.70	−48:52:16.0	1.504	375.2	12.52	0.01	11.58	0.006	11.08	0.007	0.07	3.46	M star	NTT
2	16:40:35.80	−48:51:06.0	0.777	369.5	13.43	0.016	12.45	0.01	11.90	0.010	0.04	1.85	Disk	NTT
3	16:40:34.90	−48:50:48.0	1.524	363.2	13.64	0.018	12.84	0.012	12.62	0.014	0.44	2.24	Disk	NTT
4	16:40:33.40	−48:50:23.0	1.015	353.6	13.52	0.017	12.74	0.011	12.50	0.014	0.35	1.49	Disk	NTT
5	16:40:32.20	−48:53:23.0	0.614	341.8	15.38	0.04	14.56	0.029	14.23	0.032	0.25	3.65	HMS	NTT
6	16:40:32.00	−48:49:12.0	1.439	365.2	13.58	0.017	12.73	0.011	12.30	0.012	0.13	1.2	Disk	NTT
7	16:40:31.90	−48:53:12.0	0.426	336.7	14.20	0.023	13.37	0.016	13.12	0.019	0.41	2.31	...	NTT
8	16:40:31.50	−48:53:12.0	0.616	332.3	13.63	0.018	12.74	0.011	12.21	0.012	−0.02	0.86	Disk	NTT
9	16:40:31.40	−48:52:12.0	1.719	321.6	16.45	0.095	14.94	0.048	14.62	0.059	0.95	10.98	Disk	NTT
10	16:40:31.10	−48:52:49.0	0.745	324.2	14.29	0.024	13.45	0.016	13.21	0.019	0.43	2.43	...	NTT
11	16:40:31.00	−48:49:38.0	0.797	346.1	14.92	0.033	13.96	0.021	13.39	0.022	−0.01	1.55	...	NTT
12	16:40:30.70	−48:52:15.0	0.682	316.3	14.09	0.022	12.60	0.011	11.36	0.008	−0.63	3.45	Disk	NTT
13	16:40:30.70	−48:50:26.0	0.573	327.5	15.17	0.037	14.35	0.026	14.00	0.030	0.22	4.1	HMS	NTT
14	16:40:30.20	−48:51:09.0	0.632	314.4	14.65	0.029	13.61	0.018	13.21	0.019	0.36	3.97	...	NTT
15	16:40:30.20	−48:49:59.0	1.424	331.4	17.51	0.117	16.81	0.106	16.53	0.129	0.23	0.28	...	NTT

Notes.
[a] VLT adaptive optics data indicate this source is a double.
FLAGS: VLT = data are from the Very Large Telescope, reduction discussed in Comerón & Schneider (2007). NTT = data are from New Technology Telescope, reduction discussed in Comerón et al. 2005. AAA, UAB, UAU, AAU, etc = data are taken from 2MASS with these listed photometry codes for the JHK channels, respectively: A– error < 10.9%, B – error < 15.6%, E – This category includes detections where the goodness-of-fit quality of the profile-fit photometry was very poor, U – upper limit.
(This table is available in its entirety in a machine-readable format. A portion is shown here for guidance regarding its form and content)

Figure 13). However, as discussed in Section 6.4, the Class I status derived from this color index is dubious since most of the Class I candidates are OB star candidates and the empirical colors used for class determination come from low-mass stars.

We cannot detect transition disks since we lack 24 μm data. The IRAC data are also not very deep, complete to about magnitude 12 in channel 1 [3.6 μm]. This is about magnitude 12 in K_s for a Class III object. These are identified as having

Table 11
IRAC Detections of X-Ray Sources in the RCW 108 Field

SRC #	Offset (arcsec)	Offaxis (arcsec)	Ch1	Ch2	Ch3	Ch4	Ch1e	Ch2e	Ch3e	Ch4e	IR Class
East											
1	0.481	375.2	10.51	10.13	9.88	9.42	0.01	0.01	0.02	0.05	II
2	0.447	369.5	11.06	10.75	10.40	9.90	0.02	0.02	0.03	0.03	II
3	0.421	363.2	12.50	12.53	12.72	...	0.03	0.03	0.12	...	...
4	0.373	353.6	12.14	12.10	...	...	0.04	0.05	...	...	...
6	0.441	365.2	11.46	11.05	10.60	9.79	0.01	0.01	0.03	0.03	II
7	0.364	336.7	12.88	...	...	...	0.02	...	...	...	...
8	0.233	332.3	11.41	11.05	10.72	9.84	0.01	0.01	0.03	0.05	II
10	0.063	324.2	13.20	13.18	13.61	...	0.04	0.04	0.27	...	...
11	0.261	346.1	...	12.26	...	...	...	0.03	...	...	...
12	0.382	316.3	10.99	10.62	10.06	8.46	0.01	0.01	0.02	0.03	II
16	0.476	307.2	11.32	11.31	11.26	11.35	0.01	0.01	0.05	0.10	III
17	0.322	298.2	13.30	13.17	...	...	0.04	0.06	...	...	...
18	0.425	313.4	12.85	12.84	...	...	0.03	0.04	...	...	...
19	0.524	298.2	12.39	12.39	12.51	...	0.02	0.03	0.11	...	...

(This table is available in its entirety in a machine-readable format. A portion is shown here for guidance regarding its form and content)

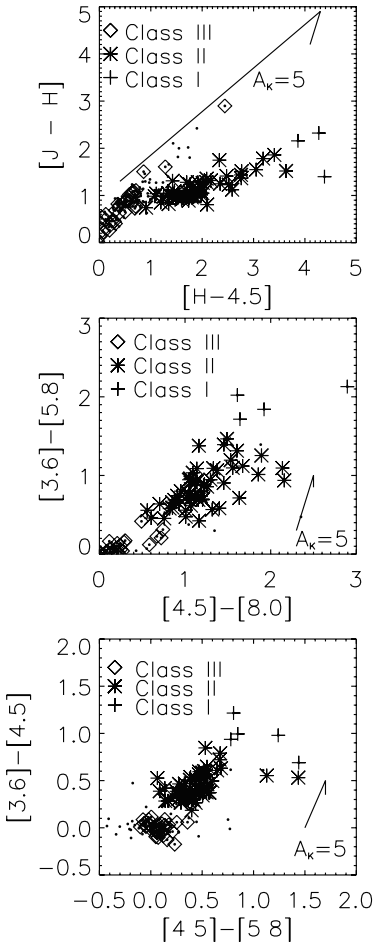

Figure 13. Plot of near- and mid-infrared colors for 236 sources with detections by 2MASS and IRAC. Class I sources are indicated by "+," Class II by "*," Class III sources are diamonds. Sources of unknown type or suspected galaxies are marked with small dots.

[3.6]–[5.8] and [4.5]–[8.0] colors of near zero, <0.4 and <0.75, respectively. Assuming a distance modulus of 10.6, this is about abs(K) = 1.4 or about 1.2 $M_{\odot}$ at 1 Myr (Siess et al. 2000). One result of the shallow nature of the IRAC map is a bias toward detecting stars with disks. Hence, even in the nominally older eastern region, 68% of IRAC detected sources for which disks class could be determined were found to have disks; meanwhile no Class III objects were detected in RCW 108–IR. Because of biases inherent in the shallow IRAC data, we focus on the deeper *JHK* data for most of the further analysis.

6.2. A_V–N_H Relation

If the IR data are of high enough quality ($Mag_{err} < 0.2$) they allow a tentative extinction estimate. Following Wolk et al. (2006), we simply calculate the amount of reddening required to move the object from the observed location on the *JHK* color–color diagram to a location consistent with zero reddening. The zero reddening location is different for a star with and without a disk and varies depending on spectral type for pure photospheres. To calculate the extinction, we first assume the least absorbed case, that all the stars have disks and deredden the photometric colors until they intersect the cTTs locus (Meyer et al. 1997). This is the only possible solution for stars outside the pure reddening box (Lada & Adams 1992). We calculate the extinction for stars inside the box for each of three hypotheses (disk, M star, or higher-mass star; HMS). For stars which lie either below the cTTs locus of to the left of the main sequence or outside of the pure reddening box by more than 2σ, no estimate of extinction is possible. The error in the extinction estimate of stars under the higher mass hypothesis is larger because the angle between the ZAMS and the extinction curve is very shallow.

To choose among the three hypotheses we use the measured N_H column. In our previous work (Wolk et al. 2006) we found $N_H/A_V = 2.0 \times 10^{21} cm^{-2}$. This is intermediate to results derived using *ROSAT* data (Ryter 1996) and those of Vuong et al. (2003).[10] The expected N_H is calculated for each of the three hypotheses noted above and the one with the minimum difference with the fitted N_H is chosen as the "correct" extinction.

[10] $N_H/A_V = 1.6 \times 10^{21} cm^{-2}$ was found by Vuong et al. (2003). This value lead to the same result, in terms of hypothesis choice, but has a larger residual, in terms of the value of A_V as derived from N_H minus the A_V measure directly from the IR data (Wolk et al. 2006).

Table 12
Bulk Near-IR Extinction and Hydrogen Column by Region

Region	Number of good fits	Mean A_V	MAD	Rejected	Mean N_H ($\times 10^{22}$ cm^{-2})	MAD	Rejected
North	8	4.58	1.11	2	0.67	0.17	2
South	16	3.31	0.36	3	0.92	0.12	3
East	35	3.01	0.22	6	0.75	0.06	2
West	22	4.66	0.44	2	0.84	0.09	1
RCW 108–IR	36	10.99	1.01	1	1.98	0.20	2
Field	117	4.07	0.23	29	0.92	0.05	22

One hundred and twenty-nine stars have both good JHK_s measurements (with K_s errors $< 7\%$ in about 100 cases and $<20\%$ in all cases) and X-ray spectral fit residuals of $<30\%$. The mean deviation between the A_V calculated by converting the N_H column and the values calculated with the color–color diagram technique (with outliers removed) was about 0.45 visual magnitudes. The A_V and the preferred model hypothesis (disk, M star, higher-mass star) are listed in columns 13 and 14 of Table 10. In cases where the N_H is not constrained by at least 50% by the X-ray spectral fits, no preference is given ("–") and the minimum A_V is listed in the table.

We can test the robustness of our results by comparison with extinction measurments published by Comerón et al. (2005). They publish extinctions for six sources in our "inner" region using the Rieke & Lebofsky (1985) extinction law and the $(H - K_s)$ color index. In all cases, our results show less extinction that that reported by Comerón et al. (2005) The mean difference was 2.8 ± 1.3 magnitudes of visual extinction. An explanation for some of the deviation is that all of the comparison stars are assumed by Comerón et al. to be O or B stars, while our data found that three of the stars lacked sufficient precision to deredden the stars in a manner consistent with their being an O star. In terms of the K-band luminosity the differences are small, less than 0.2 magnitudes at K_s.

The extinctions and hydrogen columns for the stars with good X-ray spectral fits are summarized in Table 12. In this table, column 1 indicates the source region, Column 2 indicates the number of sources in the region with N_H error < 0.3 and photometric errors below 20%. Columns 3–5 list the mean A_V, MAD, and the number of 2σ outliers in each region. Columns 6–8 list the mean N_H, MAD and the number of 2σ outliers. The N_H values listed here differ slightly from those listed in Table 9 since measurement error and not flux rate is used as the inclusion criteria. Among the high-quality measurements with N_H errors $< 30\%$ and photometric errors $< 7\%$, 75 (58%) are found to be most consistent with having an optically thick disk at K_s. These are much higher rates than indicated by the Q parameter alone but below the IRAC-determined rates. The disk fraction is highest in RCW 108–IR 65% (24/37), but not significantly so. This may indicate a bias in bright X-ray sources possessing disks. This would run counter to results from the Orion nebula studies which found X-ray sources with disks to be systematically fainter than those without disks (Kastner et al. 2005). It is more likely an age effect. We note that only 37 of 105 sources in the eastern region were bright enough for X-ray spectral fits with residuals of $<30\%$. Meanwhile 47 of 76 X-ray sources in RCW 108–IR could be fitted at that level of accuracy. Overall we obtain a higher disk rate, 70% if we additionally limit ourselves to the 42 cases in which the net number of X-ray counts exceed 100. The fraction of optically thick disks as determined by the Q parameter is 12% under these restrictions.

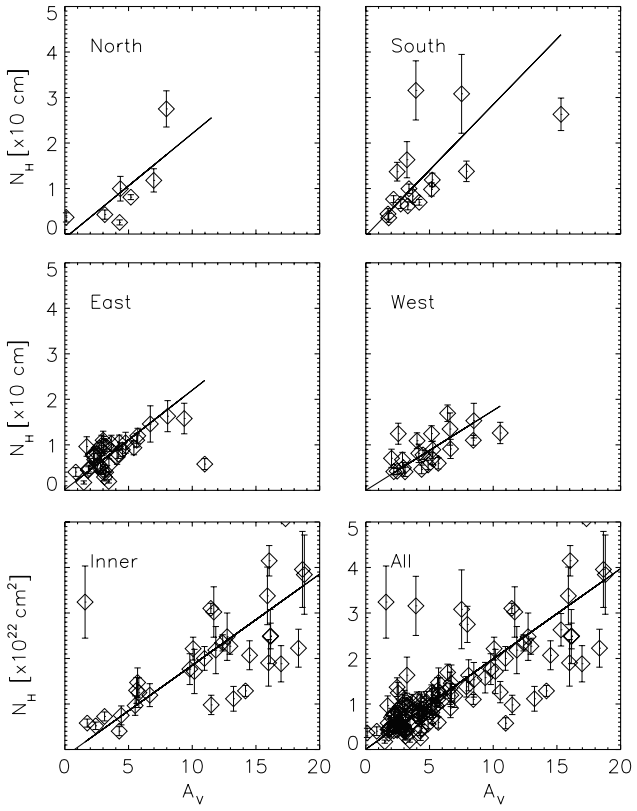

Figure 14. Plot of extinction derived from JHK colors versus N_H column. Hydrogen column is measured via X-ray spectral fits, these have been used to choose from various possible NIR extinction measures. The lines are fits to the data.

This indicates there is no bias in the Q parameter with respect to the X-ray data.

The derived values of N_H and A_V were compared among the regions. We fitted N_H as a function of A_V using an outlier-resistant two-variable linear regression,[11] weighting the variables used in the fit proportionally to their distance from the fit line. The results, summarized in Table 13, are consistent with $N_H/A_V = 2.0 \times 10^{21}$cm^{-2} and generally indicate no significant change in the gas-to-dust ratio among the regions. This is consistent with our previous result in RCW 38 (Wolk et al. 2006) of $N_H/A_V = 2.0 \times 10^{21}$cm^{-2} with a MAD of 0.29. For the present observation the region to region MADs exceed that of RCW 38, but the fit of the overall dataset is the same, with a smaller MAD.

[11] The IDL procedure robust_linefit.

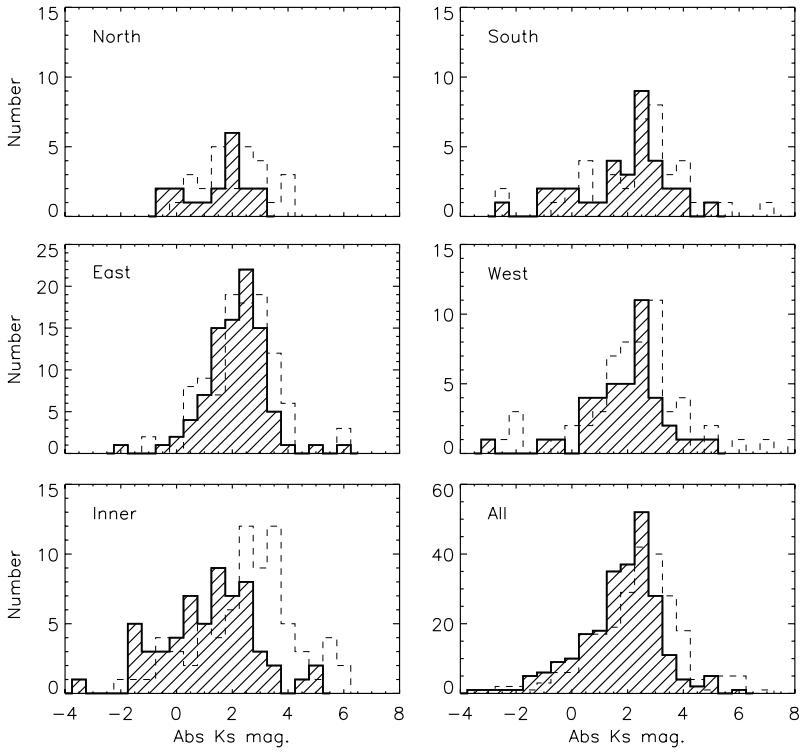

Figure 15. K_s-band luminosity functions for the X-ray sources in the RCW 108 *Chandra* field. The observed magnitudes are corrected for the distance modulus of 10.63. The hatched region in the histograms indicated the data are also corrected for the measured extinction. While the most luminous sources are all toward the inner region, there are several sources with absolute K_s magnitudes brighter than 0 in the western and southern regions.

Table 13
N_H–A_V Relation by Region

Region	Number of good fits	slope ($\times 10^{21}$)	variance[2]
North	8	2.3	0.39
South	16	2.9	0.43
East	35	2.1	0.24
West	22	1.8	0.30
RCW 108–IR	36	2.2	0.80
Field	117	2.0	0.24

However, an anomaly is seen at high values of A_V in RCW 108–IR shown in Figure 14. While the bi-square weighted fit to these data is $N_H/A_V = 2.2 \times 10^{21}$ cm^{-2}, there is a set of outliers with $A_V > 11$ and N_H significantly below the fit. Others sources at high A_V fall directly on the fit line. Two additional sources, one to the east and one to the south also fall on this secondary line. A similar behavior is seen in Serpens (Winston et al. 2007) and NGC 1333 (Getman et al. 2002, Winston et al., in preparation), where at high A_K sources seem highly depleted in gas. Winston et al. (2007) point out that an alternate possibility to gas depletion is a flattening of the reddening law at high extinction. A third possibility, which stems from the fundamental degeneracy in the fits between N_H and kT, is that the sources are at much higher plasma temperature than the X-ray fits indicate. This would require a higher N_H. In RCW 38, Wolk et al. (2006) report five sources with high quality A_V and N_H measurements with $A_V > 12$, none shows significant deviation from $N_H/A_V = 2.0 \times 10^{21}$ cm^{-2}.

6.3. The K-Band Luminosity Function

We create an intrinsic K-band luminosity function (KLF) by correcting the observed K_s band magnitude for extinction by $A_K = 0.109 \times A_V$ (Bessell & Brett 1988) and the distance modulus of 10.57. We separately construct KLFs for each of the five regions plus the overall field. We find the KLF for the full field has a mean absolute magnitude in the K_s band of 1.66 (3σ outliers excluded). However, it is clear from Figure 15, that the mean of the KLF varies from region to region. In addition to comparing the mean value of the extinction corrected K_s magnitude in each field, we examine the magnitudes which define the 90th and 10th percentiles as a way to gauge the spread in the luminosities of a given region. The break down is shown in Table 14. Here, columns 1 and 2 identify the region and the number of good corrected K_s band measurements, columns 3–5 given the mean value of K_s the MAD and the number of outliers rejected in the calculation of the mean. Column 6 is the value of K_s for the 90th percentile in the region. This value should provide a sense of the high-mass stars in each region. Column 7 is the value of K_s for the 10th percentile—this should be indicative of the completeness of each region and have less dispersion. The last column is the spread in magnitudes between the 90th and 10th percentile.

Focusing on the mean of the KLFs and the value of the 90th percentile, the data indicate that the central field is the brightest and hence most likely the youngest. It is clear that the distribution in RCW 108–IR is cut off at the faint end by dust extinction. Thus, it is plausible that the distributions in the central region is the same as for other regions. While this is plausible, it is not likely. If we assume the observations are complete in the eastern region to an absolute K_s magnitude of

Table 14
Details on the KLF by Region

Region	# -in region	Mean K_s[a]	StDev[b]	Rejected	90th percentile	10th percentile	Spread
North	18	1.48	0.26	0	−0.27	2.83	3.10
South	34	1.96	0.26	1	−0.41	3.68	4.10
East	91	2.14	0.09	4	0.94	3.21	2.27
West	41	2.07	0.20	1	0.64	3.34	2.70
RCW 108–IR	60	1.24	0.21	1	−1.06	3.17	4.43
Field	244	1.85	0.09	6	−0.15	3.21	3.36

Notes.
[a] Absolute K_s magnitude.
[b] Three sigma outliers excluded.

zero it would require that the total number of stars in RCW 108–IR cluster be at least 6 times the number of stars in the eastern region to account for the 12 sources seen in RCW 108–IR with absolute K_s magnitude <0 compared with two such sources in the eastern region. This would be more than 3000 total stars which is not compatible with the lognormal XLF shown in Section 4.3 which predicts about 800 stars in RCW 108–IR, nor the independent line of evidence that the highest-mass star in RCW 108–IR is about O8/O9 (Comerón et al. 2005). A more likely scenario is that mass segregation has deprived the sampled portion of the east region of its high-mass stars while extinction renders the fainter population of RCW 108–IR undetected in X-rays.

The southern and western fields are very similar to the eastern field with the possible inclusion of a few brighter stars from RCW 108–IR to the south. The northern field appears also to possess a mixture of stars at low absorption and high-mass stars. These results, derived primarily from the NIR data, echo the quartile results discussed in Section 3.3 as well as the regionalized results of the one-temperature spectral fits.

For all fields except the north and the south the 10th percentile is about K_s of 3.2. The 10th percentile to the south achieves $K_s \approx 3.7$, while in the north the 10th is a magnitude brighter. The similarity in the depth of the KLFs is essentially a reflection that X-ray luminosity tracks photospheric luminosity (c.f. Feigelson & Montmerle 1999 and references therein) and there is an X-ray luminosity limit in the 90 ks observation. The fact that the brightest sources are to the center is taken as evidence of the relative youth of this region. The large range in values to the south is probably indicative of some mixing, the brightest sources coming from the young, central region, while the faintest sources are from the older population.

Still it is surprising that the KLF to the south goes half a magnitude deeper than the eastern region. A point to understanding this comes from the different evolutionary timescales of the X-ray and IR flux from young stars. The *maximum* X-ray luminosity or saturation level of the corona, appears to be a function of the stellar diameter and hence is linearly related to the photospheric luminosity. But the median X-ray luminosity of G stars is the same in Orion and α Persei (Favata & Micela 2003; Güdel 2004). The X-ray observations of the RCW 108/NGC 6193 field are sensitive to similar X-ray luminosities (modulo extinction) in each region. These X-ray luminosities correspond to similar masses (following Feigelson et al. 2005). On the other hand, the K magnitudes of younger sources are brighter than their photosphere due to the contribution of disks. Hence reach lower masses. As the stars age over the first few million years, their disks vanish and the KLF tracks the photospheric luminosity. However for their first 1 Myr, a substantial fraction of the stars are over-luminous in K relative to the X-ray luminosity which is being used as the selection criteria.

6.4. Possible High-Mass Stars

Using the extinction corrected KLF we performed a survey of the cluster for O and B star candidates. On the ZAMS a star of 2.7 $M_\odot$ is a late B star. To convert the effective temperatures resulting from the models to colors, we used the conversion table from Kenyon & Hartmann (1995). Both mass and luminosity were derived from the models using the extinction corrected K_s magnitude of the X-ray selected members and the distance modulus of 10.57. On the SDF mass tracks, at 0.5 Myr a 2.7 $M_\odot$ star has an absolute K-band luminosity of −0.22 as calculated using the on-line SDF model isochrones.

We start by assuming than an age of 0.5 Myr and solar metallicity ($Z = 0.02$) is representative for RCW 108–IR due to the observed disk fraction (i.e. $Q < -0.1$). We then estimate the mass of the high-mass candidate stars independently for their corrected J, H, and K colors. This showed a trend of higher mass estimates at longer wavelength, indicative of an age underestimate. This trend was not present if we estimated the age of RCW 108–IR is 1 Myr. This age also gave consistent results for the all regions except for the eastern region where 3 Myr was found to give the most consistent results.

This leads the identification of 41 X-ray sources as candidate high-mass stars in the field, excluding the eastern region. These are listed in Table 15. Only five are stars with masses $>7M_\odot$. Three of the 41 were excluded when VLT adaptive optics data revealed that they were multiples. For the remainder, the consistency of the mass estimates among the three colors gives us confidence in the technique, although we are skeptical of the absolute age estimate due to the high measured values of A_V in RCW 108–IR. This table list the observed magnitudes, then the extinction estimate, followed by the corrected absolute magnitudes and finally the masses estimated from the absolute magnitudes.

We plot the locations of the high-mass star candidates in Figure 16. Seven of the high-mass star candidates are found just to the south of the 8 μm emission region plus an eighth source is located in the southern tip of this region. This area covers about 2.5% of the field so the fact that about 20% of the sources are found here indicates a causal relation between this region and the high-mass stars—i.e., this region itself is a subcluster of relatively recent star formation, independent of either the HD stars at the center of NGC 6193 or the core of RCW 108–IR. Note also in this region several non-X-ray detected

Table 15
Probable High-Mass Stars

SRC #	J	H	K	A_V	N_H	Abs. J	Abs. H	Abs. K	$[M_\odot]$ Est.[a]		
	Observed				($\times 10^{22}$ cm^{-2})	Ext. Corrected			J	H	K
East											
29	11.59	10.14	9.48	7.53	0.16	−1.11	−1.75	−1.93	>7	>7	>7
40	12.46	11.17	10.22	3.11	0.29	1.01	0.05	−0.70	2.2	2.5	2.7
243	8.98	8.85	8.76	0.00	0.34	−1.59	−1.72	−1.81	>7	>7	>7
245	10.15	9.74	9.54	0.00	0.16	−0.42	−0.83	−1.03	6.0	7.0	>7
North											
60	16.42	13.78	11.57	11.51	8.31	2.60	1.20	−0.27	<2	<2	3.25
61	12.56	11.23	10.48	5.18	0.81	0.52	−0.25	−0.66	3.0	3.25	3.5
146	11.70	11.13	10.85	0.31	0.37	1.04	0.50	0.24	2.5	2.5	2.7
262	12.67	11.61	11.22	4.30	0.25	0.88	0.29	0.18	2.7	2.7	2.7
RCW 108–IR											
52	15.43	13.20	11.73	11.87	2.77	1.52	0.55	−0.15	2.0	2.5	3.25
62	14.49	12.17	10.72	13.24	1.11	0.18	−0.72	−1.30	3.25	3.5	4.0
64	11.86	10.89	10.52	3.30	0.62	0.36	−0.26	−0.41	3.25	3.25	3.5
69	16.11	13.98	12.76	18.80	3.84	0.24	0.12	0.12	3.25	3.0	3.0
76	18.56	14.95	12.88	26.01	2.24	0.65	−0.17	−0.55	3.0	3.0	3.5
92	12.86	11.20	10.27	10.31	2.22	−0.61	−1.17	−1.44	3.75	4.0	4.0
100	13.65	11.95	11.13	9.81	1.77	0.32	−0.34	−0.52	3.25	3.25	3.5
111	15.47	12.85	11.52	18.34	2.23	−0.27	−0.92	−1.06	3.5	3.75	4.0
112	11.58	10.26	9.07	1.59	3.24	0.56	−0.59	−1.67	3.0	3.5	4.0
114	12.41	11.95	10.23	0.00	3.95	1.84	1.38	−0.34	<2	<2	3.25
116	13.07	11.15	10.28	12.39	2.34	−0.99	−1.59	−1.66	4.00	3.75	4.0
124	15.79	13.41	12.24	16.15	2.49	0.66	0.02	−0.11	3.0	3.0	3.0
131	13.95	11.79	10.57	12.96	2.27	−0.28	−1.05	−1.43	3.5	4.0	4.0
136	11.67	10.54	9.79	2.42	0.52	0.42	−0.45	−1.05	3.5	3.5	3.75
140	12.83	11.39	10.40	4.70	0.94	0.93	0.00	−0.68	2.5	3.0	3.5
143	12.99	11.95	11.38	4.69	0.75	1.09	0.56	0.29	2.5	2.5	2.7
144	17.88	14.62	12.79	27.35	5.78	−0.40	−0.73	−0.79	3.5	3.5	3.5
South											
54	11.71	10.94	10.65	1.39	0.39	0.75	0.12	−0.08	2.7	3.0	3.0
104	14.75	12.41	11.17	15.32	2.63	−0.14	−0.84	−1.08	3.5	3.75	3.75
222	12.91	11.85	11.40	5.16	0.98	0.88	0.38	0.26	2.7	2.7	2.7
259	8.88	8.39	8.17	2.74	0.66	−2.46	−2.66	−2.70	>7	>7	>7
263	12.72	11.67	10.94	5.84	1.19	0.50	0.07	−0.28	3.0	3.0	3.25
267	9.01	8.48	8.31	0.00	0.40	−1.56	−2.09	−2.26	>7	>7	>7
269	11.29	10.22	9.84	4.59	0.21	−0.58	−1.16	−1.24	3.75	4.0	4.0
318	12.63	11.66	11.23	5.42	0.94	0.53	0.15	0.06	3.0	3.0	3.0
West											
162	9.77	8.85	8.39	6.42	1.69	−2.61	−2.84	−2.88	>7	>7	>7
215	11.23	10.89	10.80	0.00	0.22	0.66	0.32	0.23	3.0	2.7	2.7
171	9.63	9.11	8.81	0.00	0.29	−0.94	−1.46	−1.76	4.0	4.0	>4
172	12.77	11.30	10.33	5.21	0.70	0.73	−0.18	−0.81	2.7	3.25	3.5
174	8.59	8.56	8.52	0.00	0.06	−1.98	−2.01	−2.05	5.0	5.0	5.0[b]
217	10.41	10.17	10.04	0.00	0.75	−0.16	−0.40	−0.53	3.5	3.5	3.5
286	8.91	8.69	8.25	0.00	0.01	−1.66	−1.88	−2.32	>7	>7	>7
289	13.01	11.87	11.22	3.46	0.38	1.46	0.69	0.27	2.0	2.2	2.7
296	13.67	11.96	11.23	10.55	1.26	0.12	−0.46	−0.50	3.25	3.5	3.5

Notes.
[a] Age estimated to be 1 Myr for all regions except east, 3 Myr used for east.
[b] Consistent mass estimate only found for 0.5 Myr.

possible O stars identifiable as 8 μm point sources in the *MSX* data.

About 20 of the high-mass star candidates lie in the inner/core region. Four of the high-mass star candidates are also found to be Class I protostars on the basis of there IRAC colors, especially 4.5 μm excesses. Since they are also identified as high-mass star candidates, their classification as Class I objects is not strictly applicable. This is because the empirical colors which are used for the stellar classification are drawn from low-mass stars. We speculate the luminosity of the hot stars may lead to detectable emission from cooler portions of disks than is detectable around cool stars. This gives high-mass stars with disks' IRAC colors similar to low mass protostars.

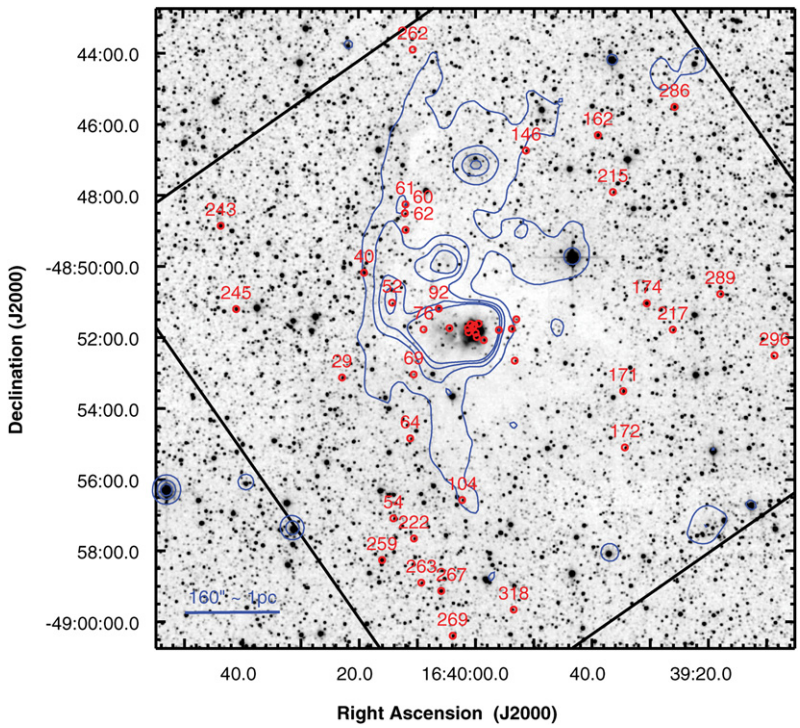

Figure 16. High-mass stars in the *Chandra* field. The large black box indicates the ACIS-I field of view. Circles indicate the locations of high-mass star candidates. The underlying image is about 6.5 pc on a side and was adapted from the 2MASS K_s data; contours are from the *MSX* A-band data. X-ray bright high mass stars are numbered except for the cluster in the central field (see Figure 17). There is also a clustering to the south. The eastern part of the field is almost free of X-ray bright high-mass stars.

Most of the 20 high mass star candidates identified here, have been previously identified as such by Comerón et al. (2005). However, Comerón et al. confined themselves to the central 30″. Of the 20 high-mass star candidates, nine (sources with IDs between 112 and 131; see Figure 16) are associated with the more active western subsection of the core and only one with the eastern subsection of the core (Src 100). The remaining sources are somewhat further from the core. Among those stars a little further from the core, Src 52 is among the most interesting as it resides in relative isolation, about 0.76 pc from the core region and 0.4 pc from the 8 μm ridge which separates the active star formation from NGC 6193, but centered on a diffuse peak of the 8 μm emission (NGC 6188). Source 52 may be the leading part of a new sub-cluster. Sources 60, 61, and 62 are also associated with enhancements in the 8 μm emission. While these sources do not appear centered on the 8 μm enhancement, Src 61 does not appear well resolved in either the X-ray or NTT observations and might be part of a complex associated with the 8 μm peak.

An age of 3.0 Myr is taken as representative for the bright stars to the east. There are 15 stars with an absolute magnitude in the K_s band consistent with being a B star in the eastern region. However, due to the non-monotonic relation between mass and IR luminosity for these photospheres, 11 of these stars are somewhat below 2.7 $M_\odot$ once data from the other colors is compared. Four stars of the ∼100 in this region, which represents a sample of the outlying region of a more evolved group of young stars are found to be high-mass stars. One of these, source 40 is very much associated with the NGC 6188 ridge and thus may be much younger and lower in mass. The bulk of the remainder of the X-ray sources are expected to comprise a fairly complete sample of the G and K membership of NGC 6193. The detection of only 3–4 high-mass star candidates to the east (including source 262 in the north), is again indicative of mass segregation in the NGC 6193 cluster.

From the X-ray perspective the high-mass stars run the gamut ranging from over 1000 counts to <16 as well as covering a wide range in kT. The overall mean (2 outliers rejected) is about 2.15 keV. About 25% of the sample is cool with one-temperature component fits below 1 keV. This is consistent with the standard model of X-rays originating in shocked material in line-driven spherically symmetric winds (MacFarlane et al. 1991). Typical temperatures in these models are about 10 MK (∼900 eV).

A similar number have temperatures above 4 keV. Hot X-ray emission from high-mass stars is a somewhat recent finding. The hard, embedded sources of RCW 108–IR resemble the central sources in NGC 2024 (Skinner et al. 2003). Schulz et al. (2001, 2003) reported temperatures of about 5 keV from Θ^1 *Orionis C*. Schulz et al. conclude that the component of the emission at this temperature must be formed "near the terminal velocity of the wind," at about 7 stellar radii from the photosphere. Gagné et al. (2005) show that they can be fitted by a two-dimensional MHD magnetospheric wind model due to ud-Doula & Owocki (2002). Several other examples of X-ray hot O and B stars have since been found (Lopes de Oliveira et al. 2006; Rakowski et al. 2006). Mullan & Waldron (2006) have proposed a two-component scenario by which the cooler X-ray emission is generated by line-driven spherically symmetric winds, and a second component of the wind emerges from magnetically active regions in polar caps which may extend as low as 45°. In such a scenario whether an O star is found to be a relatively hot or soft source may simply be a function of viewing angle.

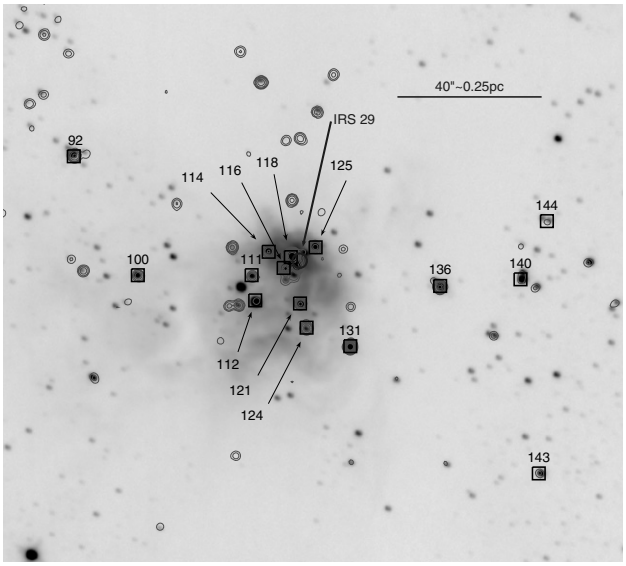

Figure 17. High-mass stars in the inner region. The field of view is about 1 pc on a side. Boxes indicate the locations of high mass star candidates in the heart of RCW 108–IR. Contours indicate X-ray count rates of 0.5, 1, 2, 4, etc counts per pixel. The underlying image is adapted from the NTT K_s data of Comerón et al. (2005). A dark lane splits the nebula. In addition to identifying the intermediate mass star candidates, IRS 29 (Straw et al. 1987) is indicated. The size of the circle is equal to the published positional error.

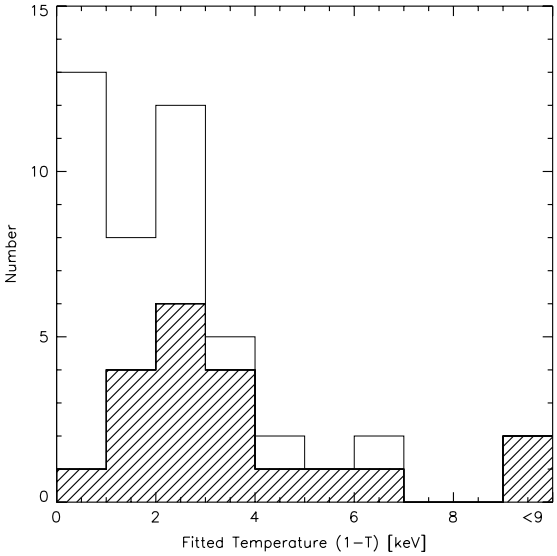

Figure 18. Histogram of the temperatures found by one-temperature spectral fits to candidate high-mass stars. Stars in the inner region (RCW 108–IR) are indicated by the hashing. These clearly represent a warmer subset of the group.

Most of the hotter stars are associated with RCW 108–IR (see Figure 18). There is a certain selection effect in RCW 108–IR where the mean temperature is about 2.8 keV (two outliers rejected) and only 1 cool high-mass star is found. This selection effect arises because local absorption can exclude the detection of bright, but soft X-ray sources when they are located deep within or on the far side the absorbing material (i.e. star forming cloud). However, the inclusion of 75% of the high-mass stars with X-ray temperature above 3 keV in the inner group indicates that young high-mass stars as observed in RCW 108–IR have hotter X-ray emission than their older, field counterparts. We note in the eastern region that all the high-mass stars have temperatures below 3 keV, including source 243 with moderate $N_{\rm H}$ and a kT of about 300 eV. In the southern region, sources 269 and the embedded source 104 are bright with kT $>$ 4. Yet the remaining high-mass star candidates all have X-ray temperatures below 1.2 keV. Nearly a quarter of the X-ray sources detected in RCW 108–IR are high-mass stars.

7. SPECIFIC INTERESTING SOURCES

While the bulk of the X-rays sources have similar characteristics, well described in a statistical sense by Tables 6, 9, and 12, there are outliers. We examined the data set of bright X-ray sources looking specifically for unusual sources which had enough counts for credible spectral fits. Of about 75 X-ray sources with 100 net counts, we found only six well fitted as plasma of $<$1 keV. Conversely, only five sources were best fitted as a thermal plasma of over 10 keV, while 13 were fitted to coronal temperature between 4 and 10 keV. Eleven sources, including six of the hot sources counted above, had measured $N_{\rm H}$ columns of greater than 2×10^{22} cm^{-2}

7.1. IRS 29

The brightest source at K was identified by Straw et al. (1987) as IRS 29. Due to the positional errors in that paper it can be associated with several possible sources (See Figure 17. We associated it with our source 118 (CXOWSBJ 164000.1–485139) as the offset is $<2''$. However 2MASS does not resolve the complex which includes Src 116 and 118 along with at least four additional K-band point sources visible in Figure 17. There is one associated 2MASS source (2MASS J16400012–4851404 about $1.87''$ away and it clearly a composite of multiple sources. Even the NTT source associated with Src 118 in Figure 17 has since been resolved. Hence it is not included in the discussion of intermediate mass stars (Comerón & Schneider 2007). It is interesting that of the six sources with log L_x $>$ 32, only IRS 29 has an identified counterpart in Table 3. It would be surprising if the primary exciting source of the H II region were IRS 29, an O9 star. Further high resolution IR observations may shed insight into this apparent discrepancy.

7.2. Cool Objects

The six sources with over 100 net counts and fitted temperatures of $<$1 keV are sources 158, 243, 254, 260, 267, and 294. Most of these have clear counterparts with moderate magnitudes in the 2MASS survey. Two (243 and 267) were identified as candidate OB stars in the previous section.

The other four may be examples of young ($\sim$3 Myr) stars with no hot coronal component. This might be indicative that a fraction (perhaps 10%) of stars no longer have a hot corona by this age (Jeffries et al. 2006). As a group they are not remarkably bright at near-IR wavelengths so we consider them probable cluster members and not foreground dKe/dMe stars.

7.3. Very Hot Objects

At the other end of the spectrum, there are five bright sources which were best fitted, by all techniques, as extremely hot. The binned data variance spectral fits as well as the unbinned C-statistic returned temperatures in excess of 10 keV. They are sources 53, 266, 281, 284, and 341. Source 53 is very hard

with no optical/IR counterpart making it a very good candidate for a background AGN. It was fitted with a power law with an index $\Gamma = 1.23 \pm 0.14$ which had a very similar reduced χ^2 to the thermal fits. Similarly sources 281 and 284 have no optical counterpart, and show fairly high extinction, ($\sim$2–5 $\times$ 10^{22} cm^{-2}), even though they are far from the active star-forming cloud, indicating that they are being seen through an absorber which lies behind the region of observed star formation. They were also fitted with a power law ($\Gamma = 0.68 \pm 0.16$ and $\Gamma = 0.21 \pm 0.42$, respectively), which had a very similar reduced χ^2 to their thermal fits. The optical/IR counterpart to source 266 is offset from the X-ray source by 1.85″ which is near the limit of our matching requirement and may be a chance superposition, this interpretation is enhanced by the high extinction observed to the X-ray source, despite the fact that it is away from the main cloud. Again, this is an indication that background absorption is being detected. The interpretation is much the same for source 341, in addition it shows a bright Fe line near 6.7 keV and is most likely an AGN.

Five (or six, see below) of the brightest 75 objects appear to be AGNs, or other hard, absorbed, non-stellar sources. Hence a little less than 10% of the bright sample of PMS "stars" are not stars at all. This is consistent with expectations derived from the Champlane survey (Hong et al. 2005). Assuming the minimum detection required an average of 10 counts, then in $\approx$90 ks, the RCW 108 observation reached a mean flux limit of about 1×10^{-15}erg s^{-1} cm^{-2} (0.5–8 keV) averaged across the field. Preliminary results from the Champlane survey for *Chandra* indicate that we can expect to find about 70 background AGNs, cataclysmic variables, neutron stars, black holes, and other non-PMS star point sources in a sample of 15 ACIS observations in the galactic plane, but not pointed at the galactic center ($90^\circ < l < 270^\circ$) sensitive to flux levels of 10^{-15}erg s^{-1} cm^{-2} from 0.5–2.0 keV. In the harder band, the result is similar. Due to the nearly opaque nature of the dust clouds in the central $\sim$40% of the field, we expect that number to be significantly lower in this field, perhaps 45 total—a little more than 10% of the total population of objects. Many of these are among the faint X-ray sources, X-ray sources with no optical/IR counterparts or the sources with offset between the X-ray position and optical/IR position exceeding 4″.

A second group of bright X-ray sources is less extreme. Thirteen have coronal temperatures between 4 and 10 keV (sources 1, 12, 70, 84, 104, 131, 151, 157, 167, 269, 278, 280, and 298). Of these, only source 280 appears to be a clear AGN, with no counterpart and high extinction. It is well fitted by a power law $\Gamma = 1.72 \pm 0.14$ with a reduced χ^2 equal to that of the one-temperature fit. Like the other AGN candidates it has no observed variability.

Several of the other hot X-ray sources (104, 131, and 269), have been identified as high-mass star candidates. Among the others, Src 131 is only about 30″ from the apparent core of RCW 108–IR (IRS 29) while Src 104 is well to the south ($\sim$2 pc) of the cluster center but lies along the same line of sight of the 8 μm diffuse emission. Source 269 is an additional 1.1 pc to the south of Src 104, but still overlaying dust absorption,

Several other hard sources (12, 70, 84, 131, 151, 167, and 298) all show strong X-ray flares while Src 278 is an X-ray variable. Temperatures of between 4–10 keV (50–110 MK) are not unusual in such flares (Favata et al. 2005). Such flares are somewhat unusual among high-mass stars; as such source 131 does seem a bit unusual but variability has been observed in other hot O stars, notably $\Theta^1 Orionis\ C$ (Schulz et al. 2001).

7.4. Very Embedded Sources

There are five additional sources that are quite absorbed but not extremely hot. Three of them—Src 116, Src 118, and Src 120—are associated with IRS 29. This has been resolved by Comerón et al. (2005) into at least six sources and by the new VLT observations into more than ten sources (Comerón and Schneider 2007). Three other components of IRS 29 have X-ray fluxes below the 100 count cutoff for quality X-ray spectra used for this analysis. In addition, Src 116 has been identified as high-mass star candidates in Section 6.4. Source 120 lacked sufficient flux at J band for classification in Section 6.4; however it was classified by Comerón et al. as a B0-B5 (their source 10) based on its H and K band colors. Our source 124 is about 15″ from IRS 29 and associated with IRS 15 of Straw et al. and source 7 of Comerón et al. which the latter group classified at B5-A0. The only outlying source (literally) in this group is source 92 (IRS 27) which is about 60″ away from IRS 29 (See Figure 17).

8. COMPARISON WITH OTHER STAR-FORMING REGIONS

Since 2000, the high resolution of *Chandra* and the large collecting area of XMM–Newton have been used to systematically study many of the active star-forming regions within 2 kpc of the Sun (see the review by Feigelson et al. 2007). *Chandra* is especially adept at younger, denser, and more embedded regions including RCW 108. Key among the contributions of these studies has been the understanding of the role of accretion and disks in flare generation as well as the impact of flares on the developing disk system. In addition, X-ray studies give us a independent pathway, relative to IR observations to evaluate cluster membership and the IMF. In this section, we discuss the relationship of the observed results from RCW 108 in the context of these global questions.

Nominally, the presence or absence of a K-band-emitting inner disk does not appear to affect X-ray emission. However, the presence of accretion appears to have negative impact on X-ray production (Flaccomio et al. 2003; Stassun et al. 2004; Preibisch et al. 2005). This is manifested as a statistical decrease in X-rays by a factor of 2–3 in accreting versus non-accreting PMS stars which are otherwise similar. In these observations, we are sensitive to the K-band excesses, but not the accretion indicators as a result of high optical absorption and the paucity of near-IR spectra. We have 17 sources with $Q < -0.10$ indicative of a thick disk and good X-ray spectra with errors in $N_{\rm H}$ and kT $<$ 33%. The log average luminosity of these sources is 31.05 ± 0.41 erg s^{-1}. There are 130 X-ray source with similar quality spectra and $Q > -0.10$, the log average luminosity of these sources with no indication of a disk is 30.87 ± 0.47. While the sources with thick disks appear brighter, the difference is less than 1 standard deviation. Overall, we only detected about one-third of the $Q < -0.10$ (disk-possessing) stars known in the field. From this we can conclude that accretion is not the primary X-ray production mechanism since this sample should include the most active accretors and viewing angle effects should not absorb X-rays on two thirds of the population unless disk flaring exceeds about 60°.

Selecting sourced with $Q > 0.0$ so that we are clearly looking at disk-free stars does not change the average flux

significantly. Among the 17 X-ray bright sources with thick disks, 3 flared (17.6%), and they were among the brighter 50% of the flares. Among the 120 X-ray bright sources with high Q, 7 flared (5.8%). The statistics flatten out a bit if we include X-ray sources with flares; no such flares are seen among the 20 such sources with low Q, but 9 are seen among the 120 fainter X-ray sources with high Q. It would appear that the presence of a disk is conducive to strong flares, but may suppress our ability to see weaker flares, or suppress the mechanism of weaker flares altogether. We re-examined the data from RCW 38 to look for this effect and found flares among 11 of 172 (∼6%) of stars with high Q. This is a slightly higher rate in an observation that was about 10% longer. But there were no flares among the 23 stars with $Q < -0.10$. So while weak flares certainly seem suppressed in stars with disks in RCW 38 as well, there were no corresponding strong flares.

In other comparisons with RCW 38, despite the fact that RCW 108 field has 75% the number of X-ray sources *and* is closer, the regions as a whole, are comparable. We estimated between 1,400 and 2,400 total members of RCW 38. The current full RCW 108 *Chandra* field contains 1400–1800 sources because it includes members of up to three separate star forming regions, including a large contribution from NGC 6193, which is probably similar in number to RCW 38 based on the two O6 stars near its center. There is evidence that the O4-5 star in the center of RCW 38 is triggering a new generation of star formation. RCW 108–IR appears to owe its triggering to the O6 stars in NGC 6193 and contains of order 800 stars. However, due to the highly variable extinction the sampling of the stars near the cluster center is much less uniform as manifest in the very choppy KLF shown in Figure 14 for RCW 108–IR.

The similarities continue when we examine the high-mass star population. In RCW 38, Wolk et al. (2006) identified 31 high-mass star candidates in the field, consistent with the number of high-mass stars expected for a cluster with about 2000 members. We detect 15 high-mass star candidates in RCW 108–IR for which we project about 800 candidates. This is in concurrence with the result of Comerón et al. (2005) and it is very consistent with the results in RCW 38. The overall finding of about 42 high-mass star candidates in the RCW 108 *Chandra* field indicates that the mass function may be a little weighted toward high-mass stars relative to RCW 38 and its surroundings. This is especially notable in light of the evidence that the sample from NGC 6193 is depleted in high-mass stars due to mass segregation. We estimate in Section 4.3 that the south and west regions contained a total of about 750 PMS stars. The identification of 17 high-mass star candidates causes the regions to appear to have a top-heavy mass function.

Two comparable star-forming regions which have been recently reported on are Cepheus B (Getman et al. 2006) and IC 1396N (Getman et al. 2007). They were observed to a similar flux limit as the X-ray data presented here and have some physical similarities. Cepheus B is one of the most active star-forming regions within a kpc. It is an optically dark cloud subject to ionizing radiation, similar to RCW 108–IR. About 390 X-ray sources are found in Cepheus B, including 64 associated with the embedded cluster. The biggest surprise of this dataset was the somewhat lower mass XLF with an excess of low-mass ($M_{\odot} \sim 0.3$) stars relative to the ONC. Our data are not deep enough to detect such a discrepancy. Like RCW 108, the diffuse X-rays in this region are entirely attributable to the integrated contribution of fainter PMS stars. This is not surprising since the region has only one known O star and it is removed from the embedded region.

IC 1396N is a much lower mass region. Getman et al. argue that the star formation in the embedded region has been triggered via a radiation-driven implosion in which photoevaporation of the exterior of the cloud by an O star, in the case of IC 1396N about 10 pc away, induces a shock that compresses the interior leading to gravitational collapse (Reipurth 1983; Gorti & Hollenbach 2002). This is similar to the geometry seen in RCW 108 where in O6 stars HD 159135/6 are seen in the *MSX* A-band data, to be clearly evaporating the edges of the cloud and small concentrations of dust are forming interior to this (see Figures 3 and 5). Also several of the smaller mid-IR peaks do seem to be independent sites of star formation, as discussed in the previous section and as predicted by radiation-driven implosion models. An alternative approach to triggering star formation, in which the photon loading of the O stars compresses the cloud (see review by Henney 2006), is not as clearly supported by the data as the concentrations of warm dust interior to NGC 6188 appear distributed in several locations in addition to the main core of RCW 108–IR.

9. CONCLUSIONS

We observed the massive, embedded young cluster RCW 108–IR and the surrounding region using *Chandra* and in the IR using the NTT/SOFI photometry and *MSX* as well as mm wave data from SEST. Over 420 X-ray sources were detected within the $17' \times 17'$ *Chandra* ACIS-I field of view in an 88 ks exposure. We expect 90% of these to be cluster members. Near-IR counterparts were identified for 361 of the X-ray sources. We performed one-temperature spectral fits to nearly 340 X-ray sources and two-temperature spectral fits to the brighter sources. Since we used the C-statistics we describe high quality data on the basis of small error instead of standard goodness-of-fit parameters. We looked for, but did not find, biasing of kT with respect to $N_{\rm H}$. Here we summarize our results.

1. NGC 6193 is seen through a uniform, foreground absorption, while the inner region, RCW 108–IR, is embedded in a locally highly variable absorber. Further, there is a high column density cloud (∼2–5 $\times$ 10^{22} cm^{-2}) behind the observable the star-forming region through which hard AGNs are seen.
2. The warm (∼225 K) dust observed along NGC 6188 is externally heated, probably by photoionization from the O stars in NGC 6193. The dense dust in the center of RCW 108–IR remains thermally shielded, even from the stars forming within it. There is about 23.1 $M_{\odot}$ of cold dust in RCW 108–IR. This implies a total gas reservoir of about 2.3 $\times$ 10^3 $M_{\odot}$.
3. Intermediate temperatures among the sources in the western region as well as a physical connection between RCW 108–IR and IRAS 16348–4849 indicate that the X-ray sources to the west of RCW 108–IR might have formed in association with IRAS 16348–4849.
4. There is no significant hot (or X-ray-emitting) diffuse plasma within this region.
5. We find evidence of mass segregation in NGC 6193. Only three high-mass star candidates were found in the southern

portion of this cluster while the existence of over 500 total stars is inferred. In addition, if one assumes a lognormal XLF, there is a deficit of sources with $\log L_x > 31.5$ relative to sources with $31.0 > \log L_x > 30.0$. This implies that the sample is depleted in early G stars, relative to K stars.

6. The X-ray flare rate among brighter stars in the cluster is about 1 per 510 ks. This is similar to the flare rate for G stars in the Orion Nebular Cluster and for lower-mass stars in the ONC at a similar X-ray count rate. Seven of the flares have temperatures in excess of 50 MK. There is a tendency for stars with disks to show either large flares or no flares at all. The presence of a disk is conducive to strong flares, but suppresses our ability to see weaker flares.
7. The gas-to-dust ratio does not change perceptibly among the five regions and is consistent with $N_{\rm H}/A_V = 2.0 \times 10^{21}$ cm^{-2} as was found in RCW 38. However, there seems to be a change in the relation at high A_V for some stars. This indicates either a gas depletion, a flattening of the reddening law at high A_V or may be a manifestation of a fundamental degeneracy in the fitting of X-ray spectra. The astrophysical phenomena should be investigated further in other embedded star forming regions.
8. Only a small fraction (<10%) of the X-ray sources in the field have large optically thick disks as indicated by a Q parameter of > -0.1. However, the evidence indicates that a much higher fraction of stars, perhaps as high as 50%–65% do have optically thick disks. Most these disks are not luminous enough to move the stars outside of the Lada & Adams (1992) reddening bands. Data from the IRAC bands indicate an even larger fraction of the stars may have disks. This makes the region a good area for the study of transition disks.
9. Hard X-ray emission seems more common from young embedded high-mass stars than from the more dispersed population of OB stars. This may indicate an evolutionary effect in the X-ray emission from high-mass stars. Overall the region has more high-mass star candidates than expected, especially in specific regions to the south and west. This indicates that small episodic star formation is taking place independently in several locations within the field. This form of star formation is predicted by radiation-driven implosion models for star formation.

We acknowledge many helpful comments by the referee M. Gagné. This publication makes use of data products from the Two Micron All Sky Survey, which is a joint project of the University of Massachusetts and the Infrared Processing and Analysis Center, funded by the National Aeronautics and Space Administration and the National Science Foundation. CXC guest investigator program supported this work through grant GO4-5013X. S.J.W. was supported by NASA contract NAS8-03060.

Facility: CXO(ACIS), Spitzer(IRAC), SEST, 2MASS

REFERENCES

Allen, L. E., et al. 2004, ApJS, 154, 363
Beers, T. C., Flynn, K., & Gebhardt, K. 1990, AJ, 100, 32
Bessell, M. S., & Brett, J. M. 1988, PASP, 100, 1134
Caramazza, M., Flaccomio, E., Micela, G., Reale, F., Wolk, S. J., & Feigelson, E. D. 2007, A&A, 471, 645
Cash, W. 1979, ApJ, 228, 939
Chini, R., et al. 2003, A&A, 409, 235
Comerón, F., & Schneider, N. 2007, A&A, in press
Comerón, F., Schneider, N., & Russeil, D. 2005, A&A, 433, 955
Cutri, R. M., et al. 2003, The IRSA 2MASS All-Sky Point Source Catalog, NASA/IPAC Infrared Science Archive, http://irsa.ipac.caltech.edu/applications/Gator/
Favata, F., Flaccomio, E., Reale, F., Micela, G., Sciortino, S., Shang, H., Stassun, K. G., & Feigelson,, E. D. 2005, ApJS, 160, 469
Favata, F., & Micela, G. 2003, SSRv, 108, 577
Fazio, G. G., et al. 2004, ApJS, 154, 10
Feigelson, E., Townsley, L., Güdel, M., & Stassun, K. 2007, Protostars and Planets V, 313
Feigelson, E. D., et al. 2005, ApJS, 160, 379
Fitzgerald, M. P. 1987, MNRAS, 229, 227
Flaccomio, E., Damiani, F., Micela, G., Sciortino, S., Harnden, F. R. Jr., Murray, S. S., & Wolk, S. J. 2003, ApJ, 582, 398
Freeman, P. E., Doe, S., & Siemiginowska, A., 4477, 76
Freeman, P., Doe, S., & Siemiginowska, A. 2001, SPIE Proc., 4477, 76
Gagné, M., Oksala, M. E., Cohen, D. H., Tonnesen, S. K., ud-Doula, A., Owocki, S. P., Townsend, R. H. D., & MacFarlane, J. J. 2005, ApJ, 628, 986
Getman, K. V., Feigelson, E. D., Garmire, G., Broos, P., & Wang, J. 2007, ApJ, 654, 316
Getman, K. V., Feigelson, E. D., Townsley, L., Bally, J., Lada, C. J., & Reipurth, B. 2002, ApJ, 575, 354
Getman, K. V., Feigelson, E. D., Townsley, L., Broos, P., Garmire, G., & Tsujimoto, M. 2006, ApJS, 163, 306
Getman, K. V., et al. 2005, ApJS, 160, 319
Gorti, U., & Hollenbach, D. 2002, ApJ, 573, 215
Güdel, M. 2004, A&ARv, 12, 71
Gutermuth, R. A., Myers, P. C., Megeath, S. T., Allen, L. E., Pipher, J. L., Muzerolle, J., Porras, A., Winston, E., & Fazio, G. 2007, ApJ, in press, (arXiv: 0710.1860)
Heinrich, J. 2003, Statistical Problems in Particle Physics, Astrophysics, and Cosmology in Proc. PHYSTAT 2003 Conf., (Stanford, CA: SLAC) http://www.slac.stanford.edu/econf/C030908 52
Henney, W. J. 2006, arXiv astro-ph/0602626
Herbst, W., & Havlen, R. J. 1977, A&AS, 30, 279
Hildebrand, R. H. 1983, QJRAS, 24, 267
Hillenbrand, L. A., & White, R. J. 2004, ApJ, 604, 741
Hong, J., Schlegel, E. M., & Grindlay, J. E. 2004, ApJ, 614, 508
Hong, J. van den, Berg, M., Schlegel, E. M., Grindlay, J. E., Koenig, X., Laycock, S., & Zhao, P. 2005, ApJ, 635, 907
Jeffries, R. D., Evans, P. A., Pye, J. P., & Briggs, K. R. 2006, MNRAS, 367, 781
Kaltcheva, N. T., & Georgiev, L. N. 1992, MNRAS, 259, 166
Kastner, J. H., Franz, G., Grosso, N., Bally, J., McCaughrean, M. J., Getman, K., Feigelson, E. D., & Schulz, N. S. 2005, ApJS, 160, 511
Kenyon, S. J., & Hartmann, L. 1995, ApJS, 101, 117
Lada, C. J., & Adams, F. C. 1992, ApJ, 393, 278
Lasker, B. M., Sturch, C. R., McLean, B. J., Russell, J. L., Jenkner, H., & Shara, M. 1990, AJ, 99, 2019
Lopes de Oliveira, R., Motch, C., Haberl, F., Negueruela, I., & Janot-Pacheco, E. 2006, A&A, 454, 265
Maritz, J. S., & Jarett., R. G. 1978, J. Am. Stat. Assoc., 73, 194
Macfarlane, J. J., Cassinelli, J. P., Welsh, B. Y., Vedder, P. W., Vallerga, J. V., & Waldron, W. L. 1991, ApJ, 380, 564
Megeath, S. T., et al. 2004, ApJS, 154, 367
Mewe, R., Gronenschild, E. H. B. M., & van den Oord, G. H. J. 1985, A&AS, 62, 197
Meyer, M. R., Calvet, N., & Hillenbrand, L. A. 1997, AJ, 114, 288
Mezger, P. G. 1994, Ap&SS, 212, 197
Moffat, A. F. J., & Vogt, N. 1973, A&AS, 10, 135
Morrison, R., & McCammon, D. 1983, ApJ, 270, 119-122
Mullan, D. J., & Waldron, W. L. 2006, ApJ, 637, 506
Niemela, V. S., & Gamen, R. C. 2005, MNRAS, 356, 974
Ossenkopf, V., & Henning, T. 1994, A&A, 291, 943
Preibisch, T., et al. 2005, ApJS, 160, 401
Price, S. D., Egan, M. P., Carey, S. J., Mizuno, D. R., & Kuchar, T. A. 2001, AJ, 121, 2819
Rakowski, C. E., Schulz, N. S., Wolk, S. J., & Testa, P. 2006, ApJ, 649, L111
Raymond, J. C., & Smith, B. W. 1977, ApJS, 35, 419
Reipurth, B. 1983, A&A, 117, 183
Rieke, G. H., & Lebofsky, M. J. 1985, ApJ, 288, 618
Rodgers, A. W., Campbell, C. T., & Whiteoak, J. B. 1960, MNRAS, 121, 103
Ryter, C. E. 1996, Ap&SS, 236, 285
Sanz-Forcada, J., Brickhouse, N. S., & Dupree, A. K. 2003, ApJS, 145, 147
Scargle, J. D. 1998, ApJ, 504, 405
Schulz, N. S., Canizares, C., Huenemoerder, D., Kastner, J. H., Taylor, S. C., & Bergstrom, E. J. 2001, ApJ, 549, 441

Schulz, N. S., Canizares, C., Huenemoerder, D., & Tibbets, K. 2003, ApJ, 595, 365
Siess, L., Dufour, E., & Forestini, M. 2000, A&A, 358, 593
Skinner, S., Gagné, M., & Belzer, E. 2003, ApJ, 598, 375
Skinner, S. L., Zhekov, S. A., Palla, F., & Barbosa, C. L. D. R. 2005, MNRAS, 361, 191
Smith, R. K., Brickhouse, N. S., Liedahl, D. A., & Raymond, J. C. 2001, ApJ, 556, L91
Stassun, K. G., Ardila, D. R., Barsony, M., Basri, G., & Mathieu, R. D. 2004, AJ, 127, 3537
Straw, S., Hyland, A. R., Jones, T. J., Harvey, P. M., Wilking, B. A., & Joy, M. 1987, ApJ, 314, 283
Townsley, L. K., Feigelson, E. D., Montmerle, T., Broos, P. S., Chu, Y.-H., & Garmire, G. P. 2003, ApJ, 593, 874
ud-Doula, A., & Owocki, S. P. 2002, ApJ, 576, 413
Urquhart, J. S., Thompson, M. A., Morgan, L. K., & White, G. J. 2004, A&A, 428, 723
Vazquez, R. A., & Feinstein, A. 1992, A&AS, 92, 863
Vuong, M. H., Montmerle, T., Grosso, N., Feigelson, E. D., Verstraete, L., & Ozawa, H. 2003, A&A, 408, 581
Walborn, N. R. 1972, AJ, 77, 312
Weaver, R., McCray, R., Castor, J., Shapiro, P., & Moore, R. 1977, ApJ, 218, 377
in press
Werner, M. W., et al. 2004, ApJS, 154, 1
Winston, E., et al. 2007, ApJ, 669, 493
Whiteoak, J. B. 1963, MNRAS, 125, 105
Wolk, S. J., Bourke, T. L., Smith, R. K., Spitzbart, B., & Alves, J. 2002, ApJ, 580, L161
Wolk, S. J., Comerón, F., & Bourke, T. L. Handbook of Star Forming Regions Vol. II. The Southern Sky, ed B. Reipurth, submitted
Wolk, S. J., Harnden, F. R., Flaccomio, E., Micela, G., Favata, F., Shang, H., & Feigelson, E. D. 2005, ApJS, 160, 423
Wolk, S. J., Spitzbart, B. D., Bourke, T. L., & Alves, J. 2006, AJ, 132, 1100
Wolk, S. J., et al. 2004, ApJ, 606, 466